RESEARCH ARTICLE | MAY 23 2023

Suppression of deep cavity aeroacoustics at low Mach number by localized surface compliance

Muhammad Rehan Naseer ; Irsalan Arif ; Randolph C. K. Leung ; Garret C. Y. Lam

Physics of Fluids 35, 056115 (2023)
https://doi.org/10.1063/5.0148276

Physics of Fluids ARTICLE pubs.aip.org/aip/pof

Suppression of deep cavity aeroacoustics at low Mach number by localized surface compliance

Cite as: Phys. Fluids **35**, 056115 (2023); doi: 10.1063/5.0148276
Submitted: 28 February 2023 · Accepted: 5 May 2023 ·
Published Online: 23 May 2023

Muhammad Rehan Naseer, Irsalan Arif,[a] Randolph C. K. Leung,[b] and Garret C. Y. Lam

AFFILIATIONS

Department of Mechanical Engineering, The Hong Kong Polytechnic University, Hong Kong, People's Republic of China

[a]**Now at**: Department of Aerospace Engineering, College of Aeronautical Engineering, National University of Sciences and Technology, Islamabad, Pakistan.
[b]**Author to whom correspondence should be addressed:** mmrleung@polyu.edu.hk

ABSTRACT

A unique concept of utilizing localized surface compliance is proposed to suppress deep cavity aeroacoustics at a low Mach number. The core idea is to provide local absorption of the energy of aeroacoustic processes supporting cavity flow self-sustained feedback loop responsible for tonal noise generation. The concept is studied with a flow past cavity of length-to-depth ratio of 0.4 at freestream Mach number 0.09 and Reynolds number based on cavity length 4×10^4 using high-fidelity, two-dimensional direct aeroacoustic simulation. Having confirmed the replication of key aeroacoustic processes in the numerical solution through careful validation, localized surface compliance in the form of an elastic panel is strategically introduced to modify every process for cavity noise suppression. The panel natural frequency is set equal to the feedback loop characteristic frequency to facilitate its flow-induced structural resonance for energy absorption. Suppression of cavity noise pressure and power levels by 3.8 and 4.8 dB, respectively, is successfully achieved, together with an unforeseen cavity drag reduction by almost 19%. Comprehensive wavenumber–frequency analyses of the coupled aeroacoustics and flow-induced panel vibration are conducted to uncover the physical mechanism of noise suppression. The results show that the same type of aeroacoustic feedback loop occurs, but its efficacy is significantly reduced due to the exhaustion of aeroacoustic process energy to the flow-induced vibrating panel. The proposed concept is confirmed to be feasible in terms of giving remarkable cavity noise and drag suppression, yet it retains the basic problem geometry intact, which are considered important in many practical applications.

I. INTRODUCTION

Flow over a rectangular cavity has received a great deal of research interest for decades due to its prevalent occurrence in various real-world engineering applications. Different types of cavity configurations are found in many transportation systems ranging from aircraft landing gear and weapons bays (Cattafesta III *et al.*, 2008) to flow over sunroofs and windows in automobiles (Kook *et al.*, 1997). The high flow dynamic loads present in these applications may lead to structural fatigue of the cavity. The highly oscillatory flow field of aeroacoustically resonant cavity flows might adversely affect the safe departure and accurate delivery of armament stored in the weapons bay. This cavity aeroacoustic resonance problem has become more acute with a growing emphasis on store separation of smart weapons that are lighter and more compact (Cattafesta III *et al.*, 2008). Cavity configurations are also often found in other engineering applications, such as turbomachines (Ziada, Oengören, and Vogel, 2002), the steam flow system in nuclear reactors (Galbally *et al.*, 2015), and gas transport systems with side branches (Bruggeman *et al.*, 1991; Ziada, 2010). Under certain operating conditions, the unsteady flow over the cavity may excite a self-sustained oscillation that would couple with a cavity acoustic mode to generate intense flow-induced noise. The demand for accurately modeling the disparate scales of acoustic and vortical disturbances driving the oscillations, and their resultant acoustic generation, is a challenging task because there might be multiple competing resonant modes of cavity flow oscillation that must be taken into consideration. All these factors have established flow-induced cavity oscillations as a canonical control problem in fluid mechanics as well as aeroacoustics that require special attention.

Plentovich *et al.* (1993) performed a comprehensive experimental study of cavity flow operating at low to high subsonic freestream Mach numbers ($0.2 \leq M \leq 0.95$) and a wide range of Reynolds numbers ($0.2–18 \times 10^6$) based on the cavity length. They classified the characteristics of cavity flow into open, closed, and transitional types and revealed the limits of cavity dimensions expressed in terms of the

length-to-depth ratio, L/D, which segregate different types of flow responses anticipated. In the case of open cavity flow ($L/D \lesssim 8$), the shear layer bridges the cavity opening, and its impingement at the cavity trailing edge produces the tonal noise response. In the case of the closed cavity flow regime ($L/D \gtrsim 13$), the incoming flow separates at the cavity leading edge but does not possess enough energy to surpass the cavity opening. So, it reattaches onto the cavity floor before the ejection takes place toward the cavity trailing edge. In this process, no discernible acoustic signature can be produced. When transitional cavity flow occurs, the cavity dimensions lay within $8 \lesssim L/D \lesssim 13$, and the flow possesses partly both the attributions (open and closed) across this range. One common feature of the flow responses of open cavity flow is the emission of high amplitude tonal noise at discrete frequencies over large broadband levels. The characteristics of noise radiation may be categorized into shallow ($L/D > 1$) and deep cavity configurations ($L/D < 1$). This categorization was first proposed by Covert (1970) and further emphasized by Heller and Bliss (1975), as they noted the pattern of aeroacoustic coupling phenomenon in the latter differs significantly from the former. However, due to the likewise shear layer characteristic motion over the cavity opening and its interaction with the acoustic mode of the cavity volume (transverse or longitudinal mode depending on the dimensions of cavity), Rockwell and Naudascher (1978) later established the peculiar flow responses of shallow and deep open cavities as a canonical type of fluid-resonant oscillation for the observed acoustic reinforcement of the shear layer instabilities at the cavity leading edge that closes the feedback loop for self-sustained resonant flow oscillations.

Rossiter (1964) proposed a mechanism for self-sustaining shallow cavity flow oscillations and devised a simple formula for predicting the dominant oscillation frequencies. In his empirical formulation, he explained the feedback phenomenon that leads to the tonal noise emission in the presence of grazing flow over a shallow cavity. The sustaining process for the feedback loop involves the Kelvin–Helmholtz instabilities of the shear layer, which are amplified as they move downstream. Upon impingement of the shear layer on the cavity trailing edge, acoustic waves are formed, which travel toward the cavity leading edge to prop up further instabilities in the shear layer. The prevalence of this phenomenon has also been reported and validated by several experimental and numerical studies (Arya and De, 2021; Liu and Gaitonde, 2021; and Han *et al.*, 2022). In the case of a deep cavity, the outcomes of many studies (East, 1966; Ziada and Bühlmann, 1992; and Ho and Kim, 2021) suggest that the shear layer oscillation at the cavity opening excites the depthwise cavity acoustic modes. The coexistence of flow dynamic and acoustic modes promotes mutual interaction, ultimately leading to noise radiation from the deep cavity. However, apart from the differences in the mode of operation from the shallow cavity, the Rossiter formula, with some modifications, can still predict the frequencies of the deep cavity flow field (Heller and Bliss, 1975). At certain flow frequencies close to the cavity natural modes, the deep cavity resonates with the maximum acoustic output (East, 1966; Ho and Kim, 2021).

Bruggeman *et al.* (1989) suggested a feedback mechanism for fluid-resonant oscillation based on vortex sound theory, involving five processes: resonant acoustic forcing on the growth of the shear layer from the cavity leading edge; the emergence of coherent vortices through instabilities in the separated shear layer; the transfer of energy from the local flow to the acoustic field as a result of the interaction between convective vorticity and the acoustic resonance; and the net energy transfer to the cavity acoustic field, which may destabilize the shear layer and reinforce vortex coalescence at certain amplitudes and phases of the feedback at the cavity leading edge. This feedback mechanism offers a reasonable explanation for the lock-on effect observed in many deep cavity experiments (Yang *et al.*, 2009; Yokoyama, Odawara, and Iida, 2016; and Ho and Kim, 2021).

Over the years, various passive and active methods for modifying the flow pattern at the cavity leading or trailing edges have been attempted to suppress the Rossiter modes for eventual cavity noise reduction (Lee, 2010; Liu and Gómez, 2019; Li *et al.*, 2020; Abdelmwgoud and Mohany, 2021; and Mourão Bento *et al.*, 2022). Sun *et al.* (2019) used a series of flow jets at the cavity leading edge to inject different rates of momentum flux to suppress the cavity flow oscillations. They observed an amplification in the pressure fluctuation over the cavity aft wall at the lower rate of injected momentum flux, while the reduction was noticed with a significant momentum flux input at the expense of a significant increase in the input energy demand. Yokoyama *et al.* (2020) attempted to improve the actuation energy consumption of the cavity noise reduction by replacing the flow jets with continuously and intermittently driven plasma actuators at the leading edge. However, their results show that high noise reduction can be achieved with less but still formidable input power, and its effectiveness plateaus with further increases in power input. It is worth mentioning that all these noise suppression methods are flow-invasive in nature. Their applications inevitably impose severe perturbations on the growing cavity shear layer which fundamentally impair the peculiar flow characteristics of the original cavity flow. This may lead to unwanted cavity aerodynamic consequences, such as stronger turbulence production, higher flow-induced drag, and higher actuation energy consumption. Excessive noise can be excited in frequency ranges that do not exist in the original flow. However, these issues are not addressed in the respective literature.

The present study proposes and explores a unique passive deep cavity noise suppression concept that utilizes localized surface compliance exhibited in the form of an elastic panel (*EP*). The rationale behind the concept is to leverage the phenomenon of flow-induced resonant panel vibration to effectively absorb the flow energy and modify the aeroacoustic feedback processes driving fluid-resonant oscillations in a deep cavity. There are two advantages to the proposed concept. First, the panel resonant vibratory displacement is deliberately set smaller than the typical cavity dimension, so the distortion of streamlines locally around the elastic panel is minimal. Second, in structural resonance, the elastic panel acts to absorb flow oscillation energy using a reactive mechanism rather than a dissipative one, so the cavity drag may not be affected. As such, the proposed approach is expected to suppress cavity noise without causing too much damage to the original cavity flow characteristics. In this study, direct aeroacoustics simulation (DAS) using conservation element and solution element (CE/SE), supported by extensive wavenumber–frequency analysis for panel design, is employed to explore the spatiotemporal aeroacoustic–structural interaction between the cavity flow field and the vibrating elastic panel. The panel is designed to resonate with the dominant cavity Rossiter frequency for an effective flow oscillation energy absorption. It is strategically placed at different cavity locations to weaken different aeroacoustic feedback and coupling processes responsible for fluid resonant cavity oscillations. In this study, we

present a comprehensive aeroacoustic–structural interaction analysis to ascertain the effectiveness of our proposed noise suppression concept and thoroughly examine its modification of cavity flow characteristics. We also provide an analysis of the flow dynamical consequences incurred by the proposed control method. An understanding of such consequences is important in the assessment of the practicability of the proposed method in real-world engineering applications but is seldom covered in many existing literature for the same scope.

This paper is organized as follows. Section II describes the formulation of the problem and the numerical methodology adopted in the present study. Section III presents a detailed analysis of the numerical results of fully rigid deep cavity flow to identify the aeroacoustic feedback and coupling for resonant cavity flow oscillation and its noise radiation. The outcomes of the analysis are taken to form the rationale of structural and configuration designs of the elastic panel as outlined in Sec. IV. The effects of elastic panels on the development of deep cavity aeroacoustics and the study of underlying mechanisms for cavity noise suppression are detailed in Sec. V. Finally, in Sec. VI, we explore the roles of the aeroacoustic–structural responses of different elastic panel configurations in cavity noise suppression.

II. PROBLEM FORMULATION AND NUMERICAL METHODS

The present problem of interest involves complex interactions between unsteady flow, panel structural vibration, and acoustics. Hence, a numerical approach capable of resolving all these physical phenomena covering both aerodynamic and acoustic scales is required. Therefore, we adopt the DAS approach for its capability of resolving the inherent coupling between the unsteady aerodynamic and acoustic solutions with sufficient accuracy. The governing equations for aeroacoustical flow and structural solvers and their implementation strategy are briefly discussed in Secs. II A–II C.

It is a well-known fact that the development of flow past open cavity is three-dimensional in nature. However, the influence of the flow three-dimensionality to the overall sustained fluid-resonant oscillation depends on the flow Mach number and the cavity configuration. Yokoyama *et al.* (2016, 2017) carried out extensive measurements of the developing flow, at the same low Mach number as in the present study, past a three-dimensional deep cavity of the same sectional length-to-depth ratio as in the present study and a spanwise length equal to 7.5 times cavity length. Their measurements of spanwise fluctuating velocities at different streamwise locations along the cavity shear layer exhibit high degree of spatial coherency covering more than 80% of the center part of cavity spanwise length. Same level of spatial coherency was also observed in the cavity noise radiation. On the other hand, in an extensive three-dimensional calculation of a flow, at a Mach number twice the one in the present study, past another deep cavity of similar sectional length-to-depth ratio but a shorter spanwise length equal to cavity length (Ho and Kim, 2021), the results show similar high degree of spatial coherency in velocity fluctuations along the cavity spanwise direction and its noise radiation. Sun *et al.* (2017) carried out extensive calculations of shallow cavities at various subsonic Mach numbers higher than that in the present study. Their results show that the shear evolution pattern (which they referred to as Rossiter mode) is strongly coherent along the spanwise direction and find it as dominant mode across different cavity configurations. In view of all these observations, it is decided to carry out two-dimensional calculations for the present study for the sake of saving computational resources.

A. Aeroacoustical flow solver

The compressible Navier–Stokes (N–S) equations and the equation of state are solved together in the study of the present cavity aeroacoustic problem. The DAS approach is built on the conservation element and solution element (CE/SE) scheme as implemented by Lam *et al.* (2014a). The numerical framework of the CE/SE scheme intrinsically ensures stringent physical law of conservation in Eq. (1), and its emphasis on integrated treatment of flux derivatives in spatial and temporal domains warrants that the time marching of the solution is essentially free of computational dissipation. Since its inception, the CE/SE scheme has been successfully utilized to model various aeroacoustics challenges, e.g., Lam, Leung, and Tang (2014b) examined the intricacies of the execution of the CE/SE scheme and demonstrated that it is a good candidate for capturing the complex aeroacoustic feedback mechanism in the duct flow. Furthermore, Arif *et al.* (2020) have successfully used the CE/SE approach to accurately depict the characteristic features of the flow past an airfoil and explored the flow processes responsible for its tonal noise generation. For the sake of generality, all primitive flow and panel variables are described in their non-dimensional form unless otherwise mentioned. The two-dimensional normalized N–S equations in strong conservation format can be written as

$$\frac{\partial \boldsymbol{U}}{\partial t}+\frac{\partial(\boldsymbol{F}-\boldsymbol{F}_v)}{\partial x}+\frac{\partial(\boldsymbol{G}-\boldsymbol{G}_v)}{\partial y}=0, \tag{1}$$

where $\boldsymbol{U}=\left[\rho\ \rho u\ \rho v\ \rho E\right]$, $\boldsymbol{F}=\left[\rho u\ \rho u^2+p\ \rho uv\ (\rho E+p)u\right]$, $\boldsymbol{F}_v=\left[0\ \tau_{xx}\ \tau_{xy}\ \tau_{xx}u+\tau_{xy}v-q_x\right](1/Re)$, $\boldsymbol{G}=\left[\rho v\ \rho uv\ \rho v^2+p\ (\rho E+p)v\right]$, $\boldsymbol{G}_v=\left[0\ \tau_{xy}\ \tau_{yy}\ \tau_{xy}u+\tau_{yy}v-q_y\right](1/Re)$, the flow normal and shear stresses $\tau_{xx}=(2/3)\mu(2\partial u/\partial x-\partial v/\partial y)$, $\tau_{xy}=\mu(2\partial u/\partial y-\partial v/\partial x)$, $\tau_{yy}=(2/3)\mu(2\partial v/\partial y-\partial u/\partial x)$, the heat flux components $q_x=[\mu/(\gamma-1)PrM^2](\partial \mathrm{T}/\partial x)$, $q_y=\left[\mu/(\gamma-1)PrM^2\right](\partial \mathrm{T}/\partial y)$, the Mach number $M=\hat{u}_0/\hat{c}_0$, the Reynolds number $Re=\hat{\rho}_0\hat{u}_0\hat{L}_0/\hat{\mu}_0$ based on the reference length $\hat{L}_0$, the Prandtl number $Pr=\hat{c}_p\hat{\mu}_0/\hat{k}_0=0.71$, the total energy $E=p/\rho(\gamma-1)+(u^2+v^2)/2$, and pressure $p=\rho \mathrm{T}/\gamma M^2$. The non-dimensionalization of the spatial coordinates x and y, time t, density ρ, pressure p, and velocities u and v are given by $x=\hat{x}/\hat{L}_0$, $y=\hat{y}/\hat{L}_0$, $t=\hat{t}\hat{u}_0/\hat{L}_0$, $\rho=\hat{\rho}/\hat{\rho}_0$, $p=\hat{p}/\left(\hat{\rho}_0\hat{u}_0^2\right)$, $u=\hat{u}/\hat{u}_0$ and $v=\hat{v}/\hat{u}_0$, respectively. Here, the variables with hat (ˆ) refer to their dimensional quantities, whereas the subscript "0" indicates freestream conditions. The reference dimension $\hat{L}_0$ is taken as the cavity length in the present study (Fig. 1).

B. Structural solver and aeroacoustic–structural coupling

The nonlinear dynamic response of the elastic panel, indicated as *EP*, is modeled by solving the one-dimensional plate equation to the simplest approximation (Dowell, 1974). The governing equation for panel displacement, normalized with the same reference variables as in Sec. II A, can be written as

$$D_{EP}\frac{\partial^4 w}{\partial x^4}-(T_{EP}+N_x)\frac{\partial^2 w}{\partial x^2}+\rho_{EP}h_{EP}\frac{\partial^2 w}{\partial t^2}+C\frac{\partial w}{\partial t}+K_{EP}w=p_{\mathrm{ex}}, \tag{2}$$

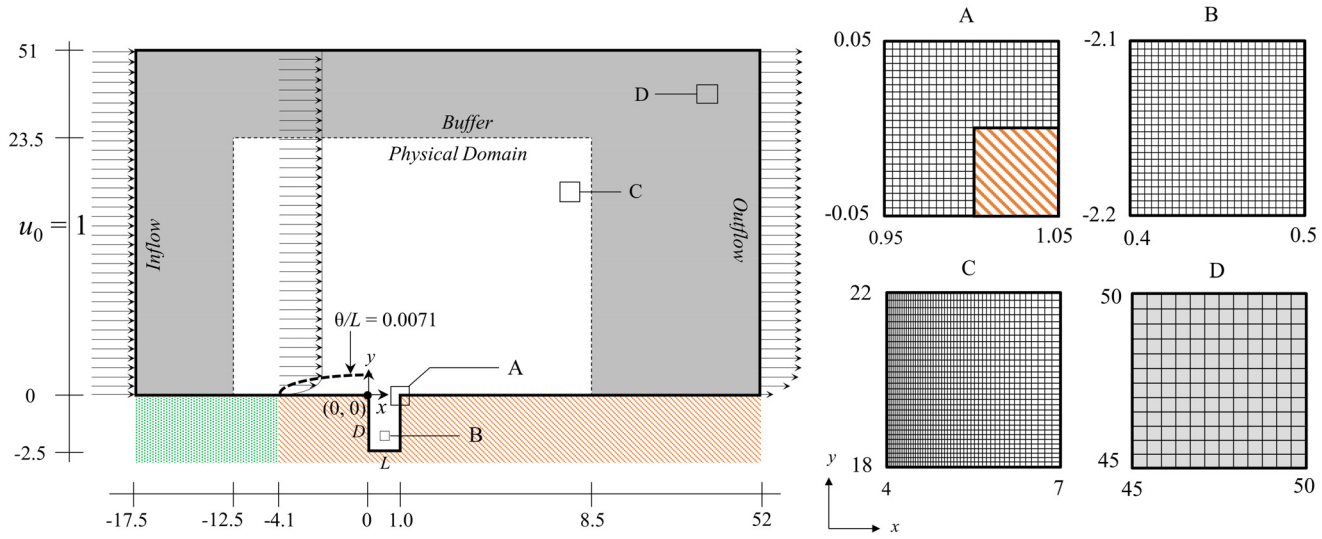

FIG. 1. Schematic sketch of the physical problem (not to scale). Zoomed views of selected regions A, B, C and D within grid G2 are given on the right.

where $D_{EP} = \hat{D}_{EP}/(\hat{\rho}_0\hat{u}_0^2\hat{L}_0^3)$ is the bending stiffness, $N_x = (E_{EP}h_{EP}/2L_{EP})\int_0^{L_{EP}}(\partial w/\partial x)^2 dx$ is the tangentially directed internal stress in response to the tensile loading, $T_{EP} = \hat{T}_{EP}/(\hat{\rho}_0\hat{u}_0^2\hat{L}_0)$ is the resultant tensile stress per unit length in the x-direction, $E_{EP} = \hat{E}_{EP}/(\hat{\rho}_0\hat{u}_0^2)$ is the elastic modulus, panel length $L_{EP} = \hat{L}_{EP}/\hat{L}_0$, panel density $\rho_{EP} = \hat{\rho}_{EP}/\hat{\rho}_0$, panel structural damping coefficient $C_{EP} = \hat{C}_{EP}/(\hat{\rho}_0\hat{u}_0)$, and the stiffness of the panel foundation $K_{EP} = \hat{K}_{EP}\hat{L}_0/(\hat{\rho}_0\hat{u}_0)$. The net pressure acting across the panel is given by $p_{ex} = \hat{p}_{ex}/(\hat{\rho}_0\hat{u}_0^2)$. Equation (2) is solved by the standard finite difference method. The nonlinear coupling between aeroacoustic fluctuation and panel structural dynamics is resolved with a monolithic scheme developed by Fan *et al.* (2018), which treats the fluid–panel system as a single entity in resolving the aeroacoustic–structural responses concurrently to maintain the two-way interaction between the unsteady flow and the panel structural dynamics. The monolithic coupling scheme is fully validated with a series of benchmark problems of aeroacoustic–structural interaction at low Mach numbers (Fan, Leung, and Lam, 2015; Fan *et al.*, 2018; and Arif, Leung, and Naseer, 2023). These works show that the coupling scheme not only possesses a superior ability to accurately resolve aeroacoustic structural coupling of increasing complexity but also gives faster convergence than the conventional partitioned approach popular in flow-induced vibration problems.

C. Physical problem and numerical setup

For the present study, a deep cavity is considered for its popularity in various fluid mechanical systems and susceptibility to flow-induced noise generation over a wide range of system operational conditions (Rockwell and Naudascher, 1978; Ziada *et al.*, 2002). That has attracted many experimental studies in cavity noise generation since then. The recent experiments carried out by Yokoyama *et al.* (2016, 2017, 2020), with a cavity of length-to-depth ratio $L/D = 0.4$ in open flow with freestream velocities ranging from 15 *m/s* to 45 m/s, have vindicated the aforesaid problem. As shown in Fig. 2, an exceptionally high noise response was observed within a limited range of inflow velocity ($25 \le u_0 \le 35$ m/s) in contrast to the lower sound pressure level (*SPL*) at 15 and 45 m/s. As such, we take the parameters of these experiments as a reference for the present numerical study. A deep cavity with $L/D = 0.4$ exposed to $u_0 = 30$ m/s is considered for its highest acoustic radiation in the experiments.

The schematic sketch of the physical problem is illustrated in Fig. 1, where the cavity leading edge is placed at the origin. A uniform flow of $M = 0.09$ and $Re = 4 \times 10^4$ based on the cavity length is allowed to enter the computational domain from the left. Combined sliding and no-slip boundary conditions are prescribed on the solid wall upstream of the cavity. A laminar boundary layer is allowed to

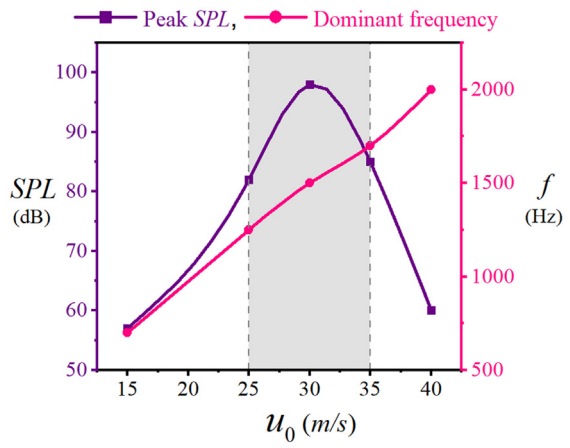

FIG. 2. Experimental acoustic response of deep cavity flow from Yokoyama *et al.* (2016, 2017, 2020).

TABLE I. Mesh parameters (minimum mesh size/maximum mesh size).

	Physical domain					Buffer zone
Mesh no. of elements	$x < -4$	$-4 \le x \le 5$	$x > 5$	$-2.5 \le y \le 0.5$	$y > 0.5$	Along x, y
G1 (coarse) 1.48×10^6	0.012/0.12	0.006/0.012	0.012/0.15	0.006/0.006	0.006/0.12	0.006/1.5
G2 (medium) 2.74×10^6	0.008/0.08	0.004/0.008	0.008/0.1	0.004/0.004	0.004/0.08	0.004/1.02
G3 (fine) 4.97×10^6	0.004/0.04	0.002/0.004	0.004/0.75	0.002/0.002	0.002/0.04	0.002/0.75

emerge from the changeover location at $x = -4.1$ and grow naturally to give momentum thickness $\theta/L = 0.0071$ at the cavity leading edge. A buffer zone stretching from physical to computational domain boundaries is applied around the physical domain to suppress any contamination due to erroneous numerical acoustic reflection. Non-reflective boundary condition proposed by Lam, Leung, and Tang (2014b) is specified at the outflow ($x = 52$) and transverse ($y = 51$) domain boundaries. The cavity and its upstream and downstream walls ($-4.1 \le x \le 52$) are made rigid with no-slip boundary conditions, while the domain length, running from the inlet to the point of boundary layer formation ($-17.5 \le x \le -4.1$), adopts the sliding wall boundary condition.

A structured grid is generated using quadrilateral mesh elements. In the application of the CE/SE scheme, a mesh element diagonally splits into four triangular elements, which makes the actual number of mesh elements four times the original size. The mesh size around the critical locations of the cavity, including leading and trailing edges (A in Fig. 1) and the cavity inside (B), are refined with special considerations for sufficiently resolving the boundary layer evolution and subsequent acoustic propagation. A grid convergence study has been carried out using three different computational grids, namely *G*1, *G*2, and *G*3, to evaluate the influence of mesh resolution in capturing the accurate flow dynamics and acoustics. Table I provides information on the mesh sizes for each grid. Grid *G*2 is generated by the refinement of *G*1, whereas the subsequent refinement of *G*2 generates Grid *G*3, and the level of refinement of each preceding mesh is equal to ∼0.5, specifically at the critical locations around the cavity. Hence, the total number of mesh elements delivered by *G*1, *G*2, and *G*3 is 1.48, 2.74, and 4.97×10^6, respectively.

Figure 3 illustrates the time history and spectra of the pressure fluctuation $p'(x, y, t) = p(x, y, t) - \overline{p}(x, y)$, where $\overline{p}(x, y)$ is the time-averaged pressure, captured at cavity bottom $(x, y) = (0.5, -2.5)$, at cavity opening (0.5, 0), and a location far away from the cavity (6.75, 21.5), for *G*1, *G*2, and *G*3. The selection of these locations is made in such a way that allows analyzing the overall mesh resolution effects encompassing the highly unsteady regions in the shear layer and cavity bottom as well as the far field location where the acoustic radiation is anticipated. Evidently, p' is fairly periodic irrespective of

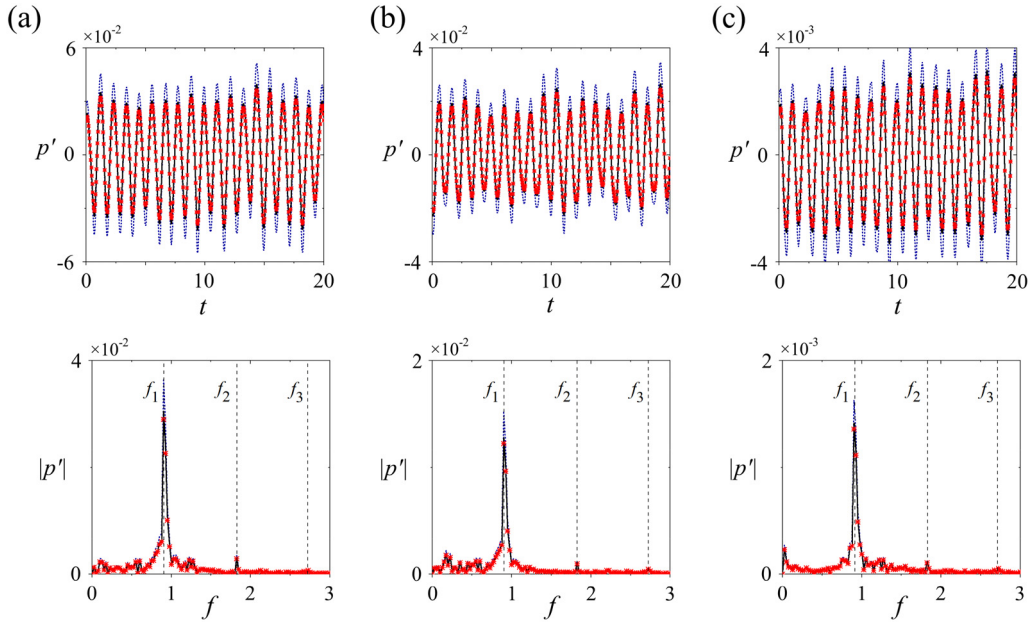

FIG. 3. Effect of grid resolution on the temporal evolution (top row) and spectra (bottom row) of pressure fluctuation p' measured at (a) cavity bottom, (b) cavity opening, and (c) far away from the cavity. Blue dotted line, *G*1; black dashed line, *G*2; red line with cross, *G*3.

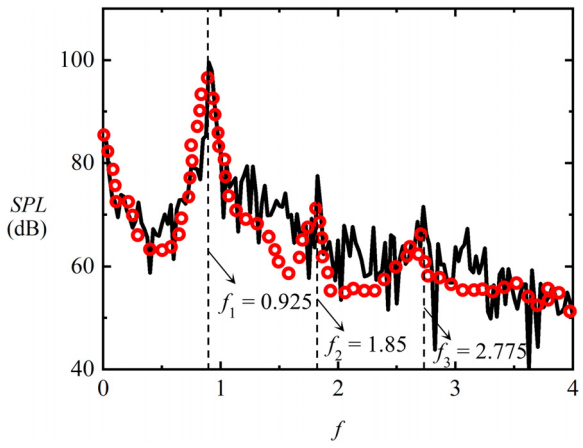

FIG. 4. Comparison of acoustic spectra at $(x, y) = (6.75, 21.5)$ obtained from the experiment of Yokoyama *et al.* (2016, 2017, 2020) and the calculation with *G*2. Black dashed line, *present study*; red circle, *experiments*.

the mesh resolution and the location of capture except for the difference in its magnitude $|p'|$. The numerical solutions of *G*2 and *G*3 stay close to each other with only a 12.1% difference, and the results appear greatly converged for these two grid configurations. However, the *G*1 exhibits a significant difference in $|p'|$ by 14.6% with reference to the *G*3. On the other hand, the acoustic pressure spectra are dominated by only one frequency $f_1 = 0.925$ in all three grid configurations, which stipulates that the main flow and acoustic features are captured even with the coarser mesh, although the magnitude of p' is compromised. Therefore, grid *G*2, with a total number of mesh elements of 2.74×10^6, is chosen in the present study for its best compromise between the accuracy and the saving of available computational resources, as the further mesh refinement beyond *G*2 gives no discernible impact on the quality of the results.

In the present study, every calculation is sufficiently advanced until a time-stationary solution is reached. Afterward, the time-marching of the solution is continued for a time episode equivalent to the 80 flow convective cycles for eventual flow dynamic and acoustic analyses. All the calculations are carried out in a parallel computing facility with 494 CPU cores for approximately 48 000 CPU hours for each case. To analyze the aeroacoustic characteristics, 2000 virtual probes are placed along the cavity walls at a separation of ~0.01 from each other. Furthermore, a total of 5400 circumferential virtual probes are placed around the cavity at radii $r = 2$, 10 and 20 for the analysis of the cavity acoustic radiation.

To validate the numerical scheme, a comparison of sound pressure level $SPL = 20 \times \log_{10}(\hat{p}'/\hat{p}_{ref})$ in dB is carried out between the numerical values and the available experimental data. The reference pressure $\hat{p}_{ref}$ is the ISO recommended value (=20 μPa) for the sound level (Bies, Hansen, and Howard, 2017). In addition, the extensive measurements of cavity flow fields in Yokoyama *et al.* (2016, 2017, 2020) show that the evolution of the large-scale structures in the shear layer covering the cavity opening is highly coherent along cavity spanwise dimension so quasi-two-dimensionality can be assumed for cavity flow and acoustic radiation. Similar features are also observed in a recent comprehensive three dimensional numerical study by Ho and Kim (2021). Therefore, it is decided to assume two dimensionality of the flow problem so that the present study can proceed at a reasonable computational cost. In order to achieve a more accordant comparison between experimental noise measurement and the present numerical results, we adopt the formulation proposed by Kato and Ikegawa (1991) and also implemented by Kusano, Yamada, and Furukawa (2020) for the estimation of *SPL* accounting for all noise generation along the entire cavity spanwise length L_{span} which is given as $SPL = SPL_{\mathrm{DAS}} + 10\log_{10}(L_{span}/\pi R)$, where the subscript DAS means the present numerical result, R is the receiver distance from the cavity, and L_{span} is taken from the experiments of Yokoyama and his coworkers. Figure 4 shows three frequencies emerge in numerical cavity noise spectrum at a far location $(x, y) = (6.75, 21.5)$ with dominant $f_1 = 0.925$, its second harmonic $f_2 = 1.85$, and third harmonic $f_3 = 2.775$. They give a constant deviation difference from experimental noise responses by 1.6% in vis-à-vis comparison (Table II). The differences in *SPL* at these frequencies are +0.6, +4.8, and +3.5 dB, respectively, from experimental values.

It is worth noting that when a flow past a cavity, a shear layer emanates from the cavity leading edge, convects across the cavity opening and impinges on the cavity trailing edge. The impingement produces an acoustic wave that travels back to the cavity leading edge and modifies the cavity shear layer formation (Rockwell and Naudascher, 1978). Such kind of feedback mechanism leads to the occurrence of a spectacular self-sustained flow oscillation across the cavity opening, known as Rossiter mode (Rossiter, 1964), which acts as the primary noise generation process for open cavity flow. Heller and Bliss (1975) modified the Rossiter prediction model and proposed the Strouhal number of the mth Rossiter mode based on cavity length L can be estimated as

$$St_m = \frac{m - \alpha}{1/\kappa + M_\infty/\sqrt{1 + (r_T/2)(\gamma - 1)M_\infty^2}}, \tag{3}$$

where r_T is the thermal recovery factor set to unity for a low Mach number flow, the quantities κ and α are, respectively, the ratio of average convection speed of disturbances in the shear layer to freestream velocity and the phase delay of acoustic wave generation at the cavity trailing edge from shear layer impingement there. With the prediction given by Eq. (3), it is informative to compare the dominant frequencies from the numerical results to ascertain if they are created by the

TABLE II. Comparison of acoustic characteristics captured at $(x, y) = (6.75, 21.5)$. The value in brackets shows the relative changes of the numerical results from respective experimental values.

	Current study	Yokoyama *et al.* (2016, 2017, 2020)	Rossiter frequency (Heller and Bliss, 1975)
$n = 1$:	$f_1 = 0.925(-1.6\%)$	$f_1 = 0.94$	$St_2 = 0.972$
	$SPL_1 = 99.6$ dB (+0.6 dB)	$SPL_1 = 99$ dB	
$n = 2$:	$f_2 = 1.85$ (−1.6%)	$f_2 = 1.88$	
	$SPL_2 = 76.8$ dB (+4.8 dB)	$SPL_2 = 72$ dB	
$n = 3$:	$f_3 = 2.775$ (−1.6%)	$f_3 = 2.82$	
	$SPL_3 = 71.5$ dB (+3.5 dB)	$SPL_3 = 68$ dB	

Rossiter modes of the present deep cavity. The two quantities, κ and α, are usually determined and their justifications are heuristic. They are often taken as 0.57 and 0.25 for open cavity flows (Gharib and Roshko, 1987; Rowley, Colonius, and Basu, 2002; and Sun *et al.*, 2017) irrespective of the operating Mach number, which makes the frequency prediction with Eq. (3) only valid at high subsonic flow conditions ($M > 0.5$). Thus, the aforementioned values of κ and α may not be applicable to the present study flow condition ($M = 0.09$). Therefore, we choose to obtain an estimate of $\kappa \sim 0.508$ from the fast Fourier transform (FFT) analysis of DAS solution as detailed in the discussion in Sec. III together with Fig. 8(b). We take the recommendation of $\alpha = 0$ from the studies of subsonic flow past deep cavity (Forestier, Jacquin, and Geffroy, 2003; Larchevêque *et al.*, 2003; and El Hassan, Keirsbulck, and Labraga, 2008). With these values of κ and α set, we find the dominant frequency f_1 agrees fairly well with the $St_2 = 0.972$ obtained from Eq. (3). One must realize that the *SPL* at f_1 is much stronger than those of f_2 and f_3 by more than 22 dB. Therefore, it can be said that only the second Rossiter mode ($m = 2$) is successfully excited and captured in the present numerical study. Similar observations are obtained from the reference experiments (Fig. 4). In summary, all the aforementioned good agreements between experimental data in the literature and present numerical results validate and verify the capability of DAS calculation in properly preserving the characteristics of the flow dynamic and acoustic responses of the chosen deep cavity in the study.

III. RIGID CAVITY AEROACOUSTICS

Although Sec. II shows a favorable agreement of the sound pressure spectra derived from the present time-stationary solution with the measured results, it is important to ensure that the present numerical study is able to correctly capture the key physical processes responsible for the aeroacoustics of the rigid cavity on which the subsequent proposed ideas of suppression are based.

The temporal variations of flow pressure fluctuation p' captured across the cavity are illustrated in Fig. 5. Periodic flow fluctuations along the shear layer region and inside the cavity are evident. For ease of illustration, the snapshots of flow dynamics are set to begin at the moment of weakest pressure inside the cavity [Fig. 5(b)]. Each successive subplot is uniformly chosen at $T/4$ difference within one period of fluctuation, $T = 1/f_1$, and captured at $(x, y) = (0.5, -2.5)$ at the dominant Rossiter frequency as appeared in Fig. 4. Figure 5(a) shows a series of concentrated periodic pressure fluctuations convecting across the cavity opening which is attributed to the peculiar flow dynamics along cavity opening.

Figure 6 shows a fluctuating shear layer emanating from the cavity leading edge and forms a series of large-scale vortical flow structures while convecting downstream as a result of Kelvin–Helmholtz instabilities. When a large-scale vortical structure impinges on the cavity trailing edge, the strong flow–structure interaction leads to the formation of separating flow from the downstream flat wall of the cavity. Simultaneously, the intensified strain rate in the vicinity of the trailing edge produces a secondary large-scale vortical structure that is stretched and swept down into the cavity (i.e., at $t = T/2$). As the secondary vortical structure detaches from the downstream corner, the strain rate there is relieved, and the high vorticity region shrinks as the flow develops with the downwash along the cavity aft wall. Further development of the shear layer stems from the repeated formation and impingement of newly formed large-scale vortical structures on the cavity downstream corner. It is important to note that the impingement of vortical structure onto the cavity trailing edge constitutes a peculiar type of vortex–corner interaction that produces an intense flow pressure fluctuation of dipolar character (Tang and Rockwell, 1983).

The pressure inside the cavity fluctuates in a clear alternating pattern in time with a spatial extent almost filling up the entire cavity [Fig. 5(b)]. The strength of the pressure fluctuation is almost two orders of magnitude weaker than that along the shear layer region. Such disparity in magnitude is typical in low Mach number aeroacoustics (Dowling and Ffowcs Williams, 1983) and the pressure fluctuation inside the cavity is likely acoustic. It is interesting to note that a strong rarefaction (pressure lower than $\overline{p}$) is released at the moment of formation of the downwash secondary vortex and the separating flow at the cavity trailing edge. A strong compression (pressure greater than $\overline{p}$) is released after these two flow processes are complete. The observations are consistent with the numerical study of a deep cavity of similar size (Ho and Kim, 2021). The pressure fluctuations are believed to constitute the acoustic resonance within the cavity which is responsible for driving acoustic waves away from the cavity (Fig. 7). An acoustic wavefront is created at the cavity opening once the cavity pressure fluctuation has attained its minimum or maximum magnitude [i.e., at $t = T/4$ or $3T/4$ in Fig. 5(b)]. The wavelength of acoustic waves tends to be $\sim$11.03, much longer than the dimensions of the cavity. Such disparity in length scale is characteristic in all low Mach number aeroacoustic problems (Dowling and Ffowcs Williams, 1983). The manifestation of characteristic length and magnitude disparity in the numerical solutions provides further evidence to the correctness and accuracy of the present numerical approach.

One has to be cognizant that the DAS solutions generally contain acoustic and flow dynamic fluctuations, but their differentiation is not obvious. This fact creates difficulty in determining the dominant physics, whether acoustic or flow dynamic, in the solutions. It is especially true in the region of cavity opening, where the acoustics are generated by the underlying unsteady flow fluctuations. To circumvent this difficulty, the combined technique for differentiation and extraction of acoustic and flow dynamic contributions in time-stationary DAS fluctuation solutions developed by Lam, Leung, and Tang (2013) is applied. In essence, it involves using the two-dimensional wavenumber–frequency spectrum ($k - f$, where k is wavenumber) for extracting the phase speeds of various fluctuation contributions followed by delineating the associated phase relationships based on the principle of the two-microphone method (Leung *et al.*, 2007). Figure 8(a) shows the $k - f$ spectrum of pressure fluctuation along a vertical line ($-2.5 \le y \le 0$) from the cavity bottom center $(x, y) = (0.5, -2.5)$. At every location on the line, the fast Fourier transform (FFT) analysis with Hamming window and zero data overlapping is applied to a temporal solution of 10^6 samples of temporal solution. The figure shows a symmetric pattern with respect to the line $k = 0$ with two peak contributions at frequency $f = 0.925$ and wavenumbers $k/2\pi = \pm 0.0838$. The phase speeds deduced from the slopes of two straight lines spanning from the peaks of the spectrum to the origin are equal to $\pm 11.03 \sim \pm 1/M$ for $M = 0.09$, but there is no signal detected along the straight lines corresponding to flow convective propagation.

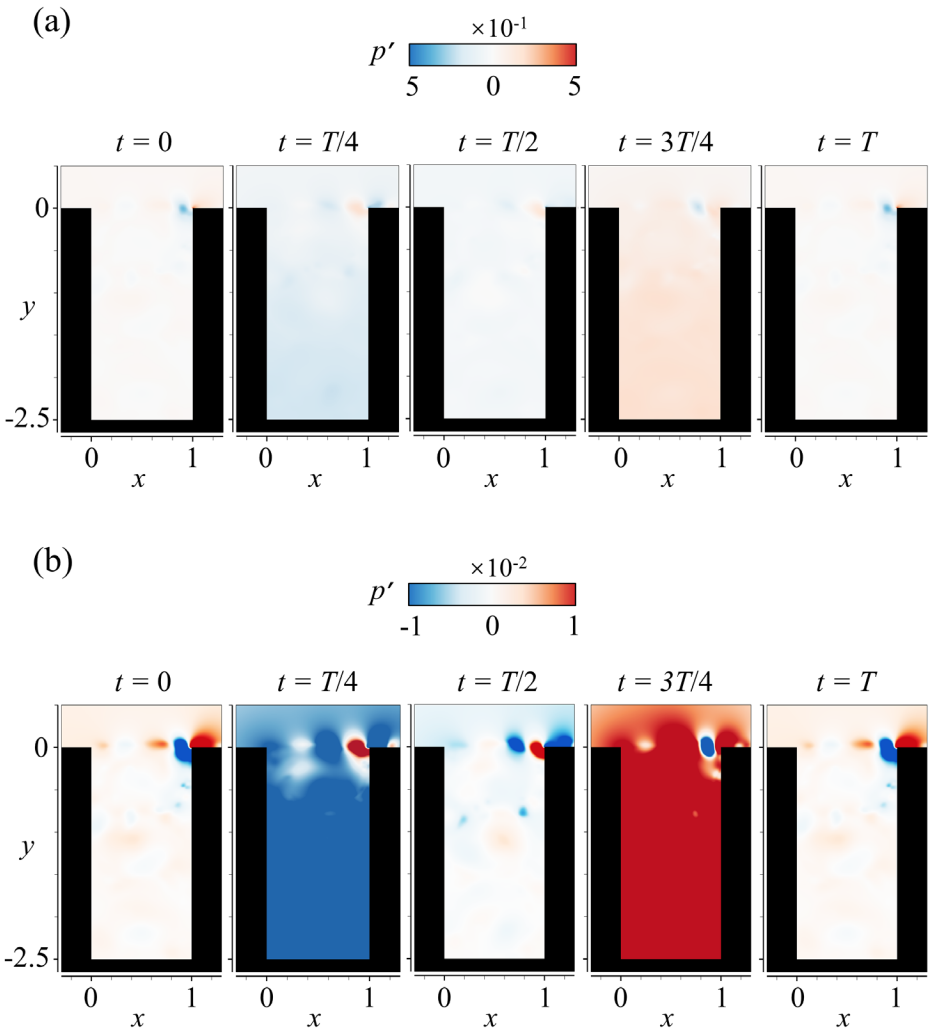

FIG. 5. Instantaneous pressure fluctuation p' around the cavity and the fluctuation scale disparity distinguishes (a) shear layer vortex strength and (b) emergence of the cavity mode.

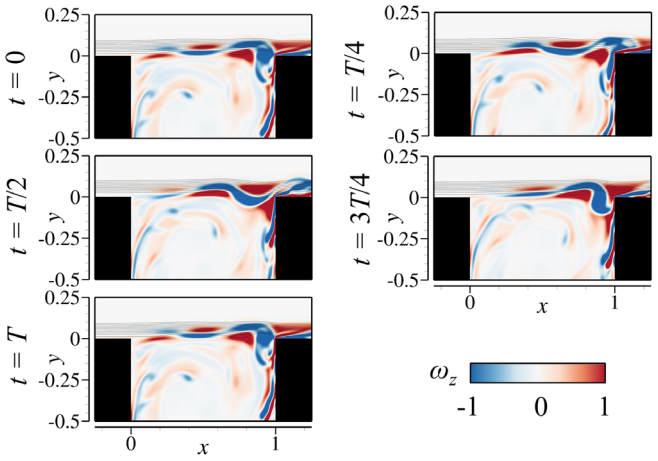

FIG. 6. Instantaneous vorticity of shear layer development near the cavity opening region.

Furthermore, Fig. 8(b) shows only one signal corresponding to the convective phase speed ∼0.508 along the downstream. These observations give two important deductions. First, the upward and downward propagating pressure fluctuations inside the cavity are purely acoustic in nature. Second, the flow fluctuation across the cavity opening is purely driven by the developing shear layer, and there is no acoustic feedback wave from the shear layer impingement propagating upstream as observed in previous studies with shallow cavities (Rossiter, 1964; Heller and Bliss, 1975; and Rowley *et al.*, 2002). However, these two types of fluctuations might interact to give aeroacoustic coupling in the flow.

The variations of the phase relationship of pressure fluctuations along the vertical line ($-2.5 \leq y \leq 5$) through the cavity bottom center are explored with reference to the pressure fluctuation at location $(x, y) = (6.75, 21.5)$ far away from the cavity. The results are illustrated in Fig. 8(c). Phase unwrapping is applied to ensure the smoothness of the data. Three regimes of phase relationship can be discerned. The first regime concerns the constant phase difference ϕ observed from the cavity bottom to $y \sim -1$, which suggests the two acoustic waves along

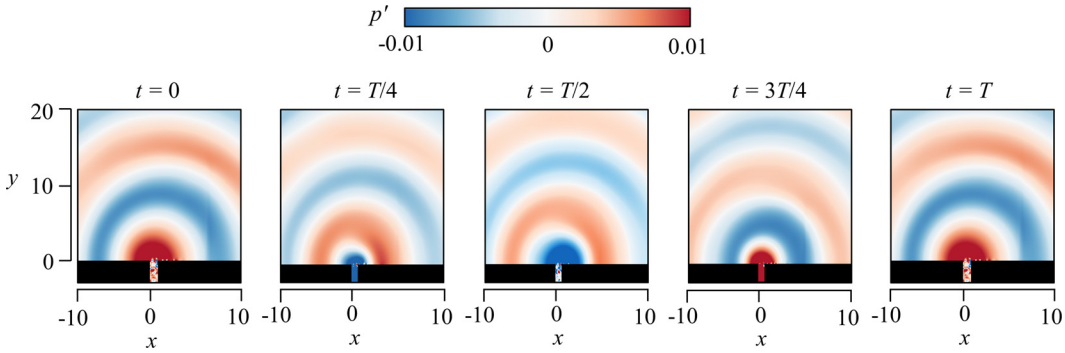

FIG. 7. Instantaneous pressure fluctuations around the cavity.

the depthwise direction are responsible for the cavity mode resonance. The second regime concerns the spatial variation of ϕ in region $y \geq 0$. There is a sharp reduction in ϕ, and its variation settles to a fairly linear one beyond $y \sim 0.5$. The linearity signifies an outgoing pressure fluctuation from the cavity opening, and its approximate gradient ϕ of variation can be used to deduce the fluctuation phase speed with the approach of Schumacher, Doolan, and Kelso (2014) and Lam and Leung (2018). A phase difference of $\pi/2$ indicates a traversal over one-quarter of fluctuation wavelength $\lambda/4 \sim 2.867$, giving a phase speed of $\sim$11.02 at the dominant Rossiter frequency f_1 observed with the propagating fluctuation. Therefore, only pure acoustic wave propagates outside the cavity, which is consistent with Fig. 7. The third regime lies within the region of $-1 \leq y \leq 0.5$, which shows a very different variation of ϕ. It reflects that the corresponding pressure fluctuations are no longer purely acoustic in nature but highly affected by the convecting shear layer across the cavity opening, giving rise to substantial nonlinear aeroacoustic interaction. Thus, this regime is aeroacoustic in nature. Figure 8(d) shows the phase difference ϕ of pressure fluctuation, with respect to the same location $(x, y) = (6.75, 21.5)$, along the cavity opening (i.e., $y = 0$). A fairly linear variation is evident within $0.1 \leq x \leq 0.85$, and its gradient gives a phase speed of $\sim$0.508, which is comparable to the convective speed of the shear layer at the cavity opening. This shows that the pressure fluctuation in this range of x is solely dominated by the evolving shear layer. The nonlinear variations of ϕ in the vicinity of two cavity edges reveal strong aeroacoustic interaction. All the variations of ϕ just discussed are similar to a recent study of the aeroacoustics of a cavity flushed mounted in a thick airfoil at a similar Mach number (Lam and Leung, 2018). It is interesting to see that all the findings from the present analysis of the DAS flow fluctuations outline a physical picture of acoustic and aeroacoustic interactions of cavity flow that is consistent with the study of Ho and Kim (2021) even though the methods of analysis are different. In what follows, the pressure fluctuations p' in acoustic (i.e., the first and second regimes) and aeroacoustic regimes (i.e., the third regime) are indicated as p'_a and p'_s, respectively.

The pressure fluctuations p'_s and p'_a along cavity opening and cavity base, respectively, are extracted for FFT analysis, and their magnitudes at the dominant frequency f_1 are illustrated in Fig. 9(a). The uniform magnitude $|p'_a|$ along the cavity bottom confirms the acoustic waves responsible for cavity mode are essentially planar and one-dimensional along the depthwise direction. The magnitude $|p'_s|$ across the cavity opening generally increases along the downstream direction due to the growth of shear layer vortices. Its pronounced rate of increase within $x \geq 0.8$ may be attributed to high unsteadiness

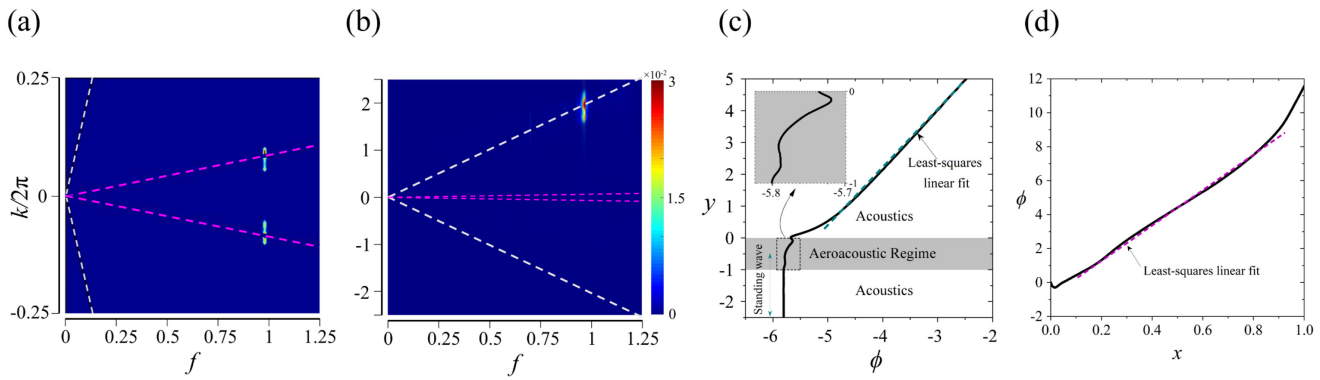

FIG. 8. Identification of dominant physical processes of cavity flow: (a) wavenumber–frequency spectra of depthwise cavity pressure fluctuation; violet and white dashed lines give convective and acoustic phase speeds, respectively; (b) wavenumber–frequency spectrum across the cavity opening at $y = 0$; (c) the phase difference between the acoustic signal at location $(x, y) = (6.75, 21.5)$ and the line running vertically through the cavity at $x = 0.5$; (d) the phase difference between the acoustic signal at location $(x, y) = (6.75, 21.5)$ and pressure signals across the cavity opening.

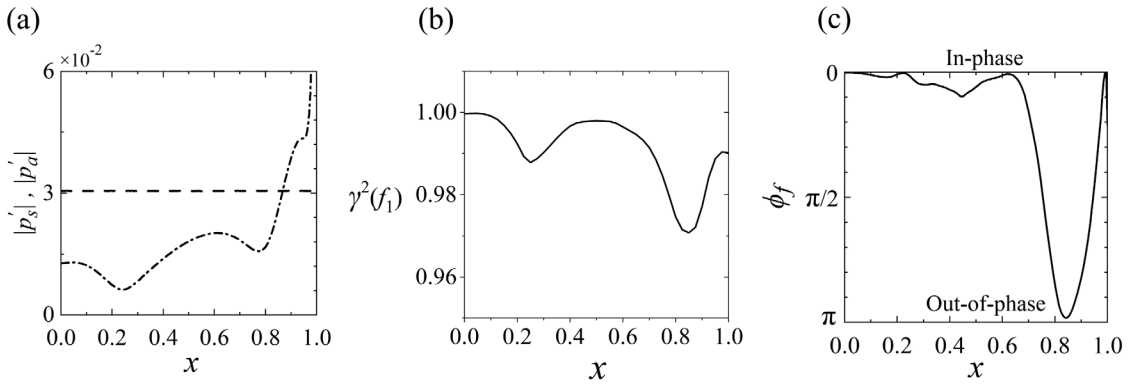

FIG. 9. Shear layer–cavity mode interaction: (a) streamwise variation of FFT pressure fluctuation across the cavity opening ($|p'_s|, - \cdot -$) and cavity bottom wall ($|p'_a|, - - -$) at dominant frequency f_1; (b) coherence between $p'_s(t)$ along $y = 0$ and $p'_a(t)$ at the cavity bottom center $(x, y) = (0.5, -2.5)$; (c) streamwise phase difference variation ϕ_f between acoustic pressure fluctuations $|p'_a|$ and shear layer pressure fluctuations $|p'_s|$ across the cavity opening.

resulting from the impingement of large-scale vortices on the downstream cavity edge (Fig. 6). Figure 9(b) presents the coherence $\gamma^2(f_1) = |P_{sa}(f_1)|^2 / P_s(f_1) P_a(f_1)$ between p'_s along $y = 0$ and p'_a at the cavity bottom center, where $P_s(f_1)$ and $P_a(f_1)$ are the power spectral densities of p' signals for the shear layer and the acoustic mode, respectively, and $P_{sa}(f_1)$ is the cross power spectral density between the signals. The coherence reveals that the pressure fluctuations are highly correlated at the dominant frequency, which implies strong coupling between the shear layer evolution and cavity mode resonance. A clearer picture of such aeroacoustic coupling is obtained from a study of the phase difference $\phi_f = \phi_s - \phi_a$ between p'_s and p'_a fluctuations at varying streamwise location x across the cavity length where the phases ϕ_s and ϕ_a are determined from FFT with respect to the same reference value [Fig. 9(c)]. The almost zero difference between ϕ_s and ϕ_a within $x < 0.65$ indicates high constructive coherence between p'_s and p'_a, which reflects the high receptivity of developing shear layer and cavity interior acoustics. Such receptivity is significantly lost within $0.65 \leq x \leq 1$, which reflects the dominance of the vortex impingement in the flow development. The entire unsteady coupling between the developing shear layer and cavity mode observed from the present numerical solutions is found to agree highly favorably with the findings of Ho and Kim (2021) despite a slightly different M and Re.

IV. DESIGN OF ELASTIC PANEL

The primary aim of the present study is to explore the feasibility of suppressing the tonal noise generated by a deep cavity using a flow-induced vibrating elastic panel. Two major design parameters of the elastic panel, namely, its mounting location and structural properties, uphold the key to achieving the said purpose. For the panel to work effectively and sustain its vibration through the flow-induced loadings, the identification of potential locations for an optimal performance requires a careful examination of the evolution of flow oscillations involved in the baseline rigid deep cavity, hereafter indicated as *RC* case. Therefore, the potential locations mounting the elastic panel are identified by deciphering the sequence and nature of the events taking place in the *RC* case.

In Sec. III, we extracted key relationships from the pressure fluctuations created by various underlying physical processes contributing to the aeroacoustic feedback for cavity noise radiation. The evidence presented helps to delineate the interactions of these processes and to seek their possible modification through our conceived ideas of elastic panel installation for the ultimate cavity noise reduction. The dominant processes identified are briefly summarized in Figs. 10(a) and 10(b). An upstream boundary layer separates from the cavity leading edge of the deep cavity and gives rise to a shear layer (process [a]) which is amplified upon convecting across the cavity opening as a result of Kelvin–Helmholtz instability. As discussed in Sec. III, the initial growth of the shear layer might be modified by the acoustic wave reflected from the cavity bottom through a certain aeroacoustic coupling (process [b]). The shear layer eventually impinges on the cavity trailing edge and splits into unsteady vorticity that downwashes along the cavity aft wall as well as undergoes further flow separation and reattachment on the horizontal wall downstream, producing strong pressure fluctuations due to intense flow–structure interaction there (process [e]). The aeroacoustic interaction of these pressure fluctuations will radiate an acoustic wave toward the cavity bottom (process [d]), which combines its reflected wave there to form a standing wave at the selected cavity mode (process [c]). As shown in Sec. III, there is no direct acoustic feedback through the shear layer excited by shear layer impingement; the processes [b] and [d] are believed to be the major contributors to the aeroacoustic coupling between the shear layer and cavity mode as similar to the views upheld by (Ho and Kim, 2021).

A. Panel location

The locations supporting various characteristic flow processes [a] to [e] are considered for elastic panel mounting [Figs. 10(a) and 10(b)]. Each panel is envisaged to act as an absorber of the energy of aeroacoustic/acoustic fluctuation of the flow process(es) concerned in such a way that the interaction with the target process will give lower cavity noise radiation. The intended actions produced by the panels are described as follows: panel *EP*1 is to modify the upstream boundary layer growth (process [a]) via flow-induced vibration; panel *EP*2 is to weaken the aeroacoustic coupling between shear layer growth and incident acoustic excitation (process [b]) via the aeroacoustic–structural interaction; panel *EP*3 is to weaken the formation of the

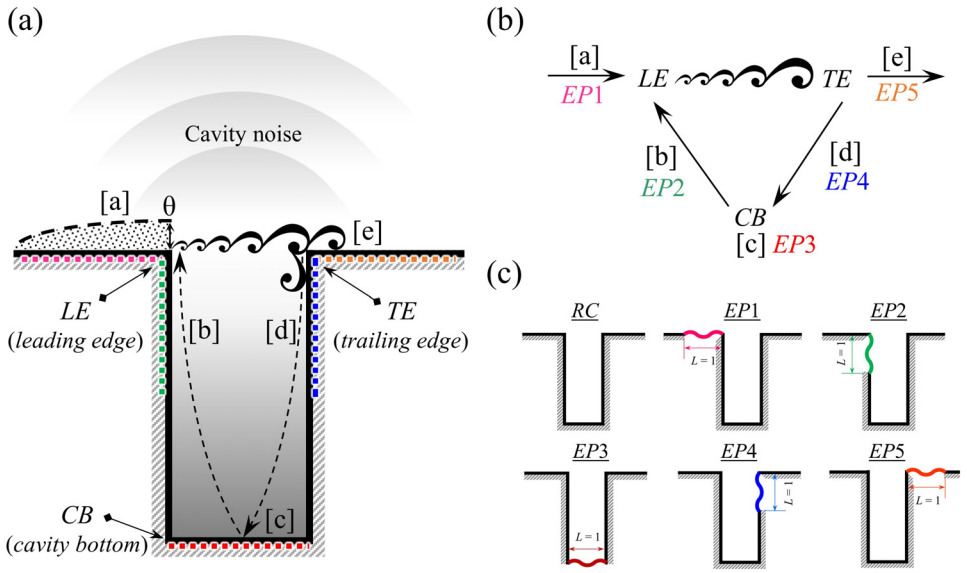

FIG. 10. Delineation of the physical processes leading to cavity noise generation and their corresponding elastic panel mounting locations: (a) schematic of the shear layer–cavity mode interaction involving the triad of *LE-TE-CB* and supported by flow processes from [a] to [e]; (b) contribution of the processes to the shear layer–cavity mode interaction; (c) selected locations of panels.

TABLE III. The rationale for the selection of panel locations.

	Leading edge (*LE*)		Cavity bottom (*CB*)	Trailing edge (*TE*)	
Target flow process	[a] Boundary layer growth	[b] Acoustically excited shear layer growth	[c] Cavity standing wave formation	[d] Cavity mode excitation by shear layer impingement	[e] Unsteady flow after shear layer impingement
Proposed panel location	*EP*1	*EP*2	*EP*3	*EP*4	*EP*5
	$-1 \le x \le 0$	$x = 0$	$0 \le x \le 1$	$x = 1$	$1 \le x \le 2$
	$-1 \le y \le 0$	$y = -2.5$	$-1 \le y \le 0$	$y = 0$	$y = 0$
Imparted panel control mode	Flow-induced vibration	Aeroacoustic–structural interaction	Acoustic–structural interaction	Aeroacoustic–structural interaction	Flow-induced vibration

standing wave inside the cavity (process [c]) via the acoustic–structural interaction; panel *EP*4 is to suppress the aeroacoustic production due to impinging shear layer (process [d]) on the panel via the aeroacoustic–structural interaction; and the panel *EP*5 is to weaken the pressure fluctuation in the vicinity of cavity trailing edge (process [e]) via flow-induced vibration. A summary of the rationale taken and the respective panel locations are given in Table III.

It must be emphasized that the mounting of all panels is targeted to modify the intricate physical processes responsible for the aeroacoustic coupling between the shear layer and cavity mode. It never aims to physically encroach the original cavity flow characteristics, so the chamfering of the cavity edges or other shape transformations as practiced previously (Saddington, Thangamani, and Knowles, 2016; Liu and Gómez, 2019; Sato *et al.*, 2019; and Yokoyama *et al.*, 2020) is not required. In fact, the proposed novel idea respects and preserves the prevalent flow processes by keeping the basic cavity shape intact and, at the same time, presents the possibility of noise reduction with strategic modification of aeroacoustic coupling through flow-induced panel vibration.

B. Panel structural properties

Table IV lists the selected parameters for all panels in the present study. The dominant flow frequency of the *RC* case is taken to be the primary parameter for consideration in the selection of panel structural properties. To accomplish the intended flow-induced panel resonance for the control purpose, the natural modal resonant frequency of every elastic panel is made the same as the dominant flow frequency. This is achieved by changing the thickness and the tension of the elastic panel accordingly. Taking into account the effect of fluid loading, the non-dimensional frequency of the nth mode of the panel

TABLE IV. Elastic panel configuration and its fluid-loaded natural frequencies.

Material	L_{EP}	ρ_{EP}	T_{EP}	h_{EP}	n	$(f_{EP})_1$	$(f_{EP})_2$	$(f_{EP})_3$	$(f_{EP})_4$
Silicon rubber	1	833.45	6.37	0.02	3	0.308	0.62	0.925	1.237

vibration, clamped at both ends, can be estimated by Eq. (4) (Blevins, 2015). All panels are assumed to be made up of elastomeric material like silicon rubber (Naseer *et al.*, 2022).

$$(f_{EP})_n = \frac{n}{2L}\sqrt{\frac{T_{EP}}{\rho_{EP}h_{EP}}}\Big/\sqrt{1+\frac{L_{EP}}{\pi n \rho_{EP}h_{EP}}}, \tag{4}$$

where L_{EP}, ρ_{EP}, T_{EP}, and h_{EP} denote the length, density, tension, and thickness of the elastic panel, respectively. In the present study, the designed frequency of the panel is taken at its third mode ($n = 3$) for meeting the natural dominant cavity flow frequency as well as the consideration of panel fabrication practicality.

V. DEEP CAVITY AEROACOUSTICS WITH ELASTIC PANEL

Figure 11 shows a comparison of cavity noise spectra captured at the location $(x, y) = (6.75, 21.5)$ far from the cavity. Tonal noise prevails in all cases, showing that the original coupling between the developing shear layer and cavity mode is not radically changed or destroyed in the presence of elastic panels. For *EP*1 and *EP*2, a mild noise reduction of 1.4 and 1.1 dB is observed at the dominant frequency $f = 0.925$, the same as in the *RC* case. The same dominant frequency also prevails in the *EP*5 case but gives a noise amplification of 2.6 dB instead. For *EP*3 and *EP*4, a remarkable noise reduction of 3.6 and 3.8 dB is observed, respectively, but they occur at a different dominant frequency $f = 1.25$, which is 35% higher than the *RC* value. Figure 12(a) shows the snapshots of instantaneous pressure fluctuation for all the configurations captured at the moment when the acoustic rarefaction hits the cavity bottom. As illustrated, the overall cavity noise radiation pattern in all the cases is similar to the *RC* case [Fig. 7(b)]. The *EP*3 and *EP*4 cases slightly skew the directivity along the downstream direction with new maximum radiation at an angle of ~45° from the downstream horizontal wall [Fig. 12(b)]. The extent of azimuthal noise reduction of *EP*1 and *EP*2 and the noise amplification of *EP*5 are fairly uniform [Fig. 12(c)]. However, the extent of noise reduction of *EP*3 and *EP*4 shows some variations. The effectiveness of noise reduction and amplification of elastic panel can be illustrated with the change of sound power level $\Delta PWL = 10\log_{10}(W_{EP}/W_{RC})$ in dB of cavity noise radiation where $W = \int_0^{\pi} p'_{rms} d\theta$, and the results are illustrated in Table V. A significant sound power reduction of almost 5 dB is possible with EP3 and *EP*4, but *EP*5 gives a very strong sound power enhancement by 3.3 dB. In summary, all these phenomena firmly reveal that the panels installed in the vicinity of the leading edge and cavity bottom (Fig. 10) give rise to mild and significant cavity noise reduction, respectively. In the vicinity of the trailing edge, where the impingement of the shear layer dominates, a panel installed inside the cavity gives significant noise reduction, but one outside the cavity gives noise amplification instead. The physical mechanisms responsible for the observed phenomena are analyzed and discussed in Secs. V A and VI.

Figure 13 depicts the distribution of the time-averaged coefficient of pressure, $\overline{C}_p = 2(\overline{p} - p_\infty)/\rho_\infty u_\infty^2$, along all the cavity walls. For all

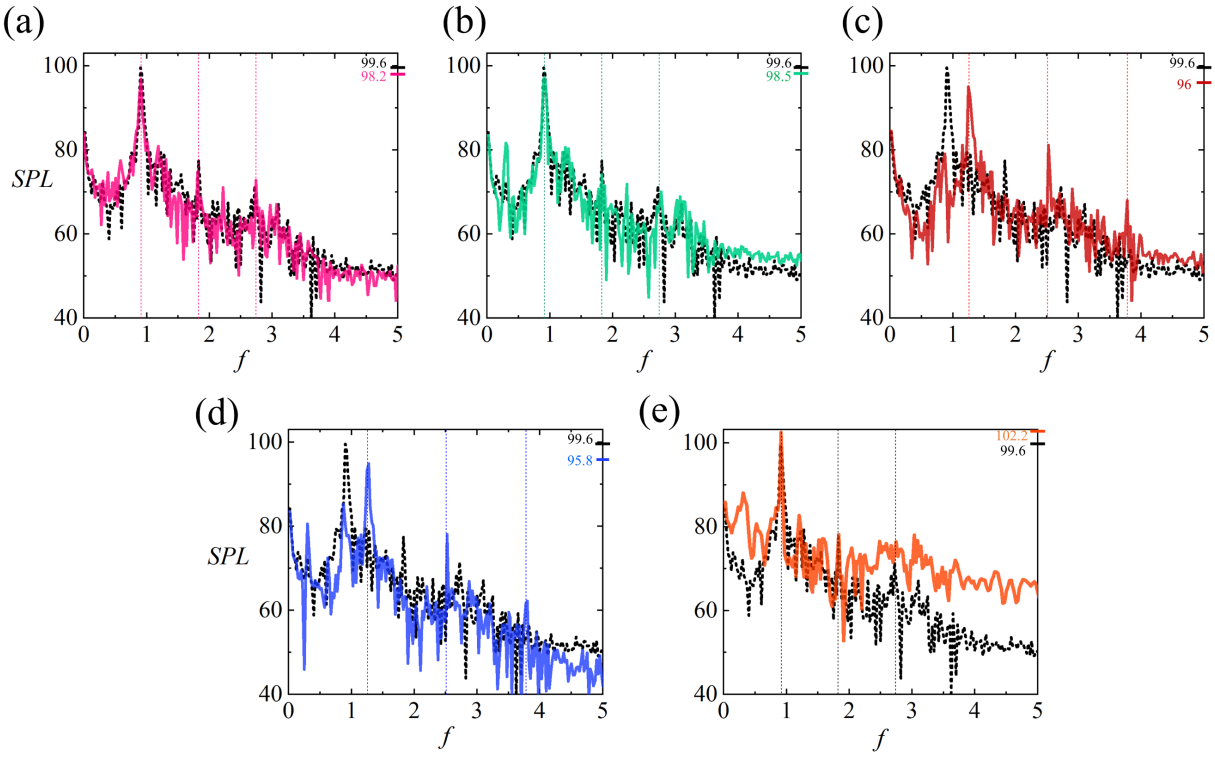

FIG. 11. Comparison of acoustic spectra at $(x, y) = (6.75, 21.5)$. The markers at the right indicate peak values: (a) *EP*1, (b) *EP*2, (c) *EP*3, (d) *EP*4, and (e) *EP*5. Dotted line: *RC*, color lines: *EP* cases.

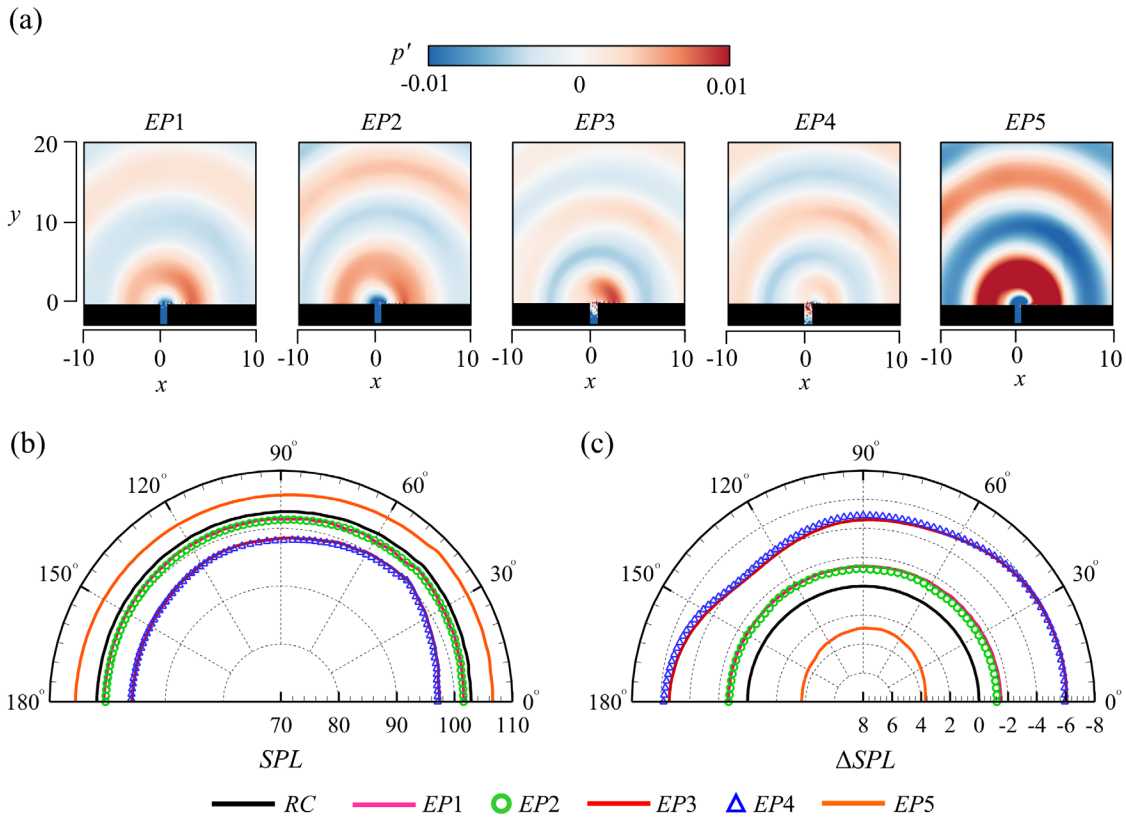

FIG. 12. (a) Instantaneous acoustic pressure fluctuations of all cases; (b) azimuthal distribution of peak *SPL* at $r = 10$; and (c) azimuthal *SPL* change, $\Delta SPL = 20\log_{10}(p'_{EP}/p'_{RC})$ at $r = 10$.

TABLE V. Change sound power level due to elastic panels.

Cases	*EP*1	*EP*2	*EP*3	*EP*4	*EP*5
ΔPWL (dB)	−1.3	−1.1	−4.6	−4.8	+3.2

EP cases, the distribution is similar to the *RC* case, each of which shows roughly uniform wall pressure and sudden spikes at locations on the vertical walls very close to the cavity leading edge and trailing edge. Generally, the retention of $\overline{C}_p$ distribution in all *EP* cases infers that the introduction of an elastic panel does not induce notable change to the normal pressure force on the walls. There is an observable $\overline{C}_p$ deviation of *EP*5 from the *RC* by ∼19.1% (along $-0.5 \geq y \geq -1.25$) and ∼19.4% (along $-0.5 \leq y \leq 0$) on the front and aft walls, respectively, which reflects a more vigorous shear layer dynamics, resulting in the overall noise amplification. Moreover, it is interesting to see the effects of elastic panels on the time-averaged drag acting on the cavity (Table VI), calculated as $\overline{C}_D = 2\overline{F}_d/\rho u^2 l_{(x,y)}$, where $\overline{F}_d = \overline{F}_{form} + \overline{F}_{fric}$; $\overline{F}_{form} = -\int_{-2.5}^{0} p(0,y)\,dy + \int_{-2.5}^{0} p(1,y)\,dy$; $\overline{F}_{fric} = \int_0^1 \tau(x,-2.5)\,dx$. In all cases, the coefficient of skin friction drag, $\overline{C}_{D,fric}$, is two orders of

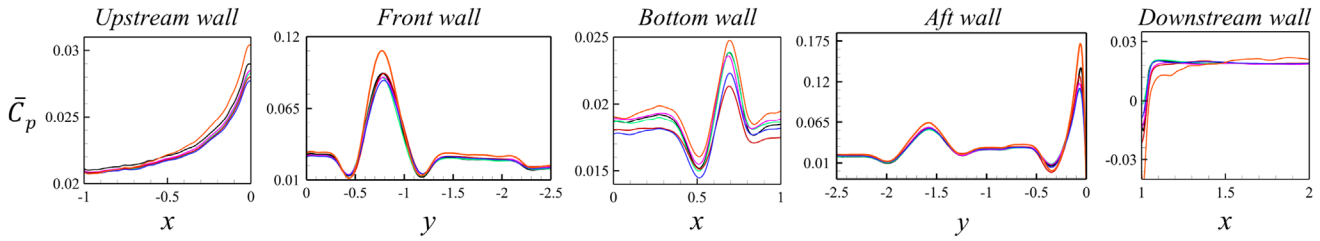

FIG. 13. Coefficients of pressure along the cavity walls. Black dashed line, *RC*; purple dashed line, *EP*1; green dashed line, *EP*2; red dashed line, *EP*3; blue dashed line, *EP*4; brown dashed line, *EP*5.

TABLE VI. Skin friction drag, form drag, and total drag comparison of all cavity configurations. Values in brackets show the percentage deviations from the *RC* case.

	Skin friction drag, $\overline{C}_{D,\ fric}$	*Form drag,* $\overline{C}_{D,\ form}$	*Total drag,* $\overline{C}_D$
RC	5.68×10^{-5}	1.70×10^{-3}	1.76×10^{-3}
*EP*1	6.38×10^{-5} (+12.2%)	1.42×10^{-3} (−16.7%)	1.48×10^{-3} (−15.7%)
*EP*2	6.50×10^{-5} (+14.4%)	1.69×10^{-3} (−0.7%)	1.75×10^{-3} (−0.2%)
*EP*3	5.48×10^{-5} (−3.6%)	1.59×10^{-3} (−6.4%)	1.64×10^{-3} (−6.4%)
*EP*4	6.48×10^{-5} (+14.1%)	1.36×10^{-3} (−20.2%)	1.42×10^{-3} (−19.1%)
*EP*5	6.31×10^{-5} (+11.1%)	2.03×10^{-3} (+19.1%)	2.09×10^{-3} (+18.1%)

magnitudes weaker than that of form drag $\overline{C}_{D,form}$, so the latter is the major contributor to total cavity drag $\overline{C}_D$. The cases *EP*1, *EP*2, *EP*3, and *EP*4 give less total drag, up to 20%, less than the *RC*. On the contrary, *EP*5 increases the total drag by almost 20%. Evidently, the proposed use of an elastic panel for noise reduction is achieved without any sacrifice in the cavity aerodynamics at all. In fact, it provides the aerodynamic benefit of lower cavity drag. That makes the present idea superior to those attempted before (Sanmiguel-Rojas *et al.*, 2011). It is interesting to note that similar aeroacoustic benefits are also observed in the study of using flow-induced elastic panels for airfoil tonal noise reduction (Arif *et al.*, 2022).

A. Modification of cavity noise generation mechanism

The variation of cavity noise observed in *EP*1 to *EP*5 cases implies that the coupling of the shear layer and the cavity mode of *RC* is greatly modified by the new possibility of acoustic- and/or aeroacoustic–structural interaction given by the elastic panel. To uncover the underlying physical mechanisms leading to the amplified and reduced cavity noise, the phase relationships of pressure fluctuations along cavity opening (i.e., along $0 \le x \le 1$ and $y = 0$) at dominant peak frequencies in all cases are examined carefully with reference to that at the cavity bottom center, using the same approach as carried out in Sec. III. It should be reminded that the discussions in Sec. III firmly establish that the pressure fluctuations across the cavity opening and at the cavity bottom are purely aerodynamic and acoustic in nature, so the same respective symbols, p'_s and p'_a, are used in forthcoming discussions.

Figure 14(a) shows the coherence between the p'_s and p'_a fluctuations for all cases. The *EP*1 and *EP*2 cases maintain more or less the same high level of coherence as *RC* along the significant part of the cavity opening length. So, the same type of coupling between the developing shear layer and the cavity mode (i.e., processes [b] and [d] in Table III) exists as observed in the *RC*. Nevertheless, there is a significant drop in coherence at $x \sim 0.125$ for *EP*3 and *EP*4 cases. Figure 14(b) shows the phase difference ϕ_f between the pressure fluctuations. It is interesting to note that the trends of ϕ_f for *EP*1, *EP*2, and *EP*5 cases are similar to the *RC* case, but their magnitudes vary. The acoustic excitation on the shear layer growth around the leading edge ($x < 0.25$) is weaker due to a deviation of ϕ_f from zero, but it becomes effective again for shear layer growth downstream $0.26 \le x \le 0.6$. The values of ϕ_f are smaller than the *RC* case within $0.6 < x \le 0.8$ but become larger up until the cavity trailing edge for stronger coupling between shear layer impingement and cavity mode in these cases. For *EP*3 and *EP*4 cases, the trends of coherence and ϕ_f of p'_s and p'_a fluctuations together show that the fluctuations are weakly synchronized. Their highly similar variations of ϕ_f give a very different trend from the other cases. Generally, their ϕ_f deviates greatly from zero except at $x \sim 0.25$ and $x \sim 0.7$. Their first minimum $\phi_f = 0.85$ occurs at $x = 0.125$. Given the exceptionally weak coherence at the same x, the fluctuations bear an extremely weak synchronization. At $x = 0.5$ and 0.9, the fluctuations are completely out of phase, so they essentially do not synchronize at all. It is believed that all the observed weakly synchronized fluctuations result in a significant weakening of the inherent coupling between the developing shear layer and cavity mode. The weakened coupling is responsible for the significantly reduced cavity acoustic fluctuation p'_a by 54% of *RC* [Fig. 14(c)] in contrast with only 16% reduction observed in *EP*1 and *EP*2 cases. It is also responsible for the variations of the shear layer pressure fluctuations p'_s in all cases with panel [Fig. 14(d)]. The p'_s in *EP*1 and *EP*2

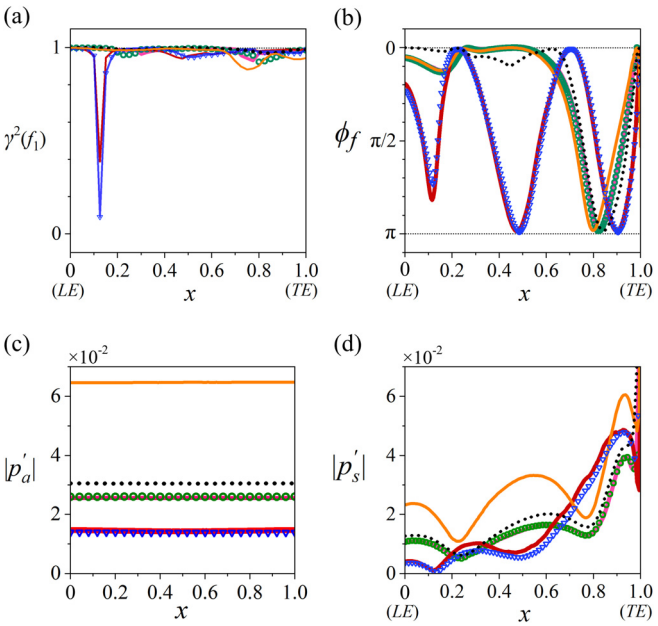

FIG. 14. (a) Coherence between shear layer pressure p'_s across the cavity opening ($y = 0$) and acoustic pressure p'_a at the cavity bottom center; (b) phase difference between p'_s and p'_a; (c) variation of FFT transformed p'_a magnitude across the cavity bottom; and (d) variation of FFT transformed p'_s magnitude across the cavity opening. Black dotted line, *RC*; purple dashed line, *EP*1; green line with circle, *EP*2; red dashed line, *EP*3; blue line with inverted triangle, *EP*4; brown dashed line, *EP*5.

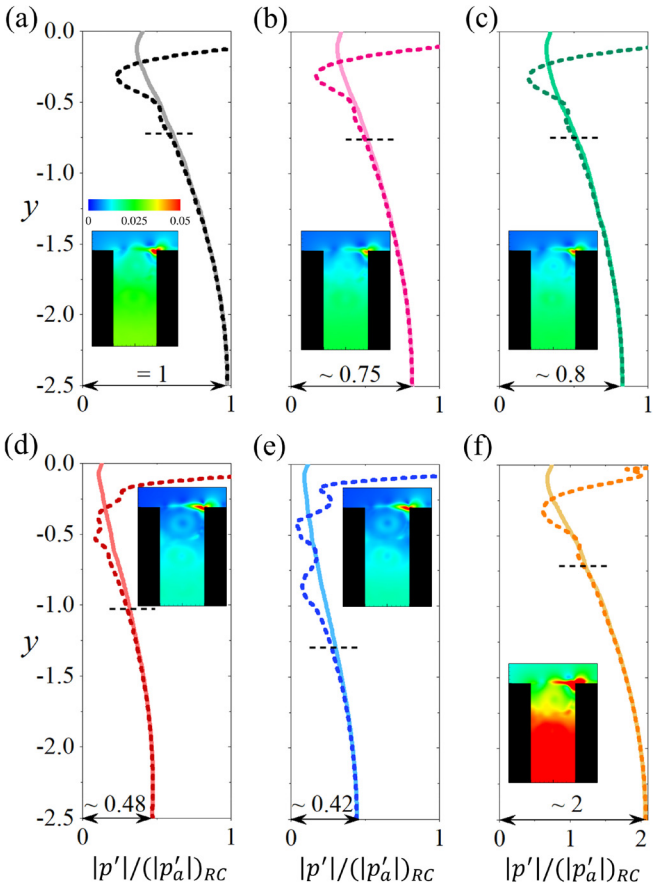

FIG. 15. FFT transformed pressure fluctuation magnitudes along the cavity front (solid line) and aft (dashed line) walls. Every color plot shows the distribution of root mean squared pressure fluctuation in the respective cases: (a) *RC*, (b) *EP*1, (c) *EP*2, (d) *EP*3, (e) *EP*4, and (f) *EP*5.

cases are consistently weaker than the *RC* case across the entire cavity opening. In *EP*3 and *EP*4 cases, the acoustic excitation on the shear layer growth is almost fully suppressed in the vicinity of the cavity leading edge, and prominent shear layer growth appears to be delayed to a downstream location $x \sim 0.25$ [supported with forthcoming discussions in conjunction with Figs. 15(d) and 15(e)]. This gives rise to a thinner shear layer of more concentrated vorticity than the *RC* case, so its impingement at the cavity trailing edge produces stronger p'_s fluctuations between $0.65 < x \leq 1$. However, due to the aforementioned weakened coupling and completely out of phase relationship between the shear layer and the cavity mode, the stronger pressure fluctuations are not effectively transformed into cavity noise radiation. The stronger pressure fluctuation p'_s in the vicinity of the cavity trailing edge is also observed in the *EP*5 case, which might be attributed to the local flow–panel interaction on shear layer impingement. Such stronger pressure fluctuation not only produces stronger acoustic excitation for more vigorous shear layer growth, an increase in p'_s by ∼100% at $x = 0$, but also amplifies cavity noise radiation through the same coupling between the shear layer and cavity mode as the *RC* case.

To apprehend the effects of panels on the coupling between the developing shear layer and the cavity mode, Fig. 15 depicts the pressure fluctuations along the cavity front and aft walls in all cases, along with the root mean square pressure distributions in colored sub-plots. In the figure, only the line plots of FFT transformed pressure magnitudes $|p'|$ are normalized by the FFT transformed acoustic pressure magnitude at the cavity bottom $|p'_a|_{RC}$ of the *RC* case. Evidently, there is a common feature in all the pressure distributions along the walls. Every pressure magnitude outlines a variation in the form of cosine function from its maximum at the cavity bottom, which substantiates the presence of an acoustic standing wave spanning from the cavity bottom. In the *RC* case, the standing wave fills almost the entire cavity, as illustrated by the pressure magnitude variation on the front wall. There is a strong nonlinear pressure variation within $y > -0.5$ on the aft wall due to the shear layer impingement. The coupling between the shear layer and the cavity standing waves between the walls is evident for the same range of y. These observations agree favorably well with the analysis by Ho and Kim (2021). The associated p'_{rms} distribution of *RC* case clearly shows the separation of acoustic and aeroacoustic regimes for cavity noise development that is consistent with the result of frequency–wave analysis discussed earlier [Fig. 8(c)]. In *EP*1 and *EP*2 cases, the weakening of the coupling between the shear layer and cavity mode is obvious with the shift of the boundary between acoustic and aeroacoustic regions down the cavity depth resulting in shorter standing wave wavelength. In addition, the magnitude of standing waves in these cases is reduced to 20%–25% of *RC* case, which implies that the acoustics inside the cavity takes less energy from flow fluctuations through coupling to buildup. The coupling further weakens in *EP*3 and *EP*4 cases as their standing wave magnitudes are reduced to 42%–48% of *RC* case. In addition, their wavelengths are further shortened, which gives a prominent shift of dominant cavity noise frequency from $f = 0.925$ to $f = 1.25$. Their associated p'_{rms} distributions show a clearer separation between acoustic and aeroacoustic regions. In the *EP*5 case, the effect of the coupling is so strengthened that it gives a standing wave of a similar wavelength as *RC* (and the same dominant cavity noise frequency) but with a significant increase in magnitude by almost doubling the *RC* value.

A careful study of all the p'_{rms} distributions, as illustrated in Fig. 15, give an interesting observation. In *RC*, *EP*2, *EP*3, and *EP*5 cases, along the direction of shear layer development $y = 0$, the contours of pressure fluctuations show substantial growth at more or less the same location inside the shear layer region. This shows that in all these cases, the coupling between the emerging shear layer and the cavity mode acoustic excitation (process [b] in Fig. 10) is effective at a location very close to the cavity leading edge. As a result, the occurrence of the associated aeroacoustic coupling processes responsible for Rossiter self-synchronized flow fluctuations is very similar, so all these cases give rise to the same dominant cavity noise frequency $f_1 = 0.925 = St_2$ from Eq. (3). However, in *EP*3 and *EP*4 cases, the growth of the shear layer appears to be delayed to a location downstream by a distance ∼0.2 from the cavity leading edge along $y = 0$. As such, the effective length for shear layer growth in these two cases is effectively shortened to only ∼0.8*L*. If we take this shorter effective shear layer length and the effective $\kappa \sim 0.498$ from the (k–f) spectra across the cavity opening in *EP*3 and *EP*4 cases for the calculation of Eq. (3), it is surprising to see the St_2 obtained is equal to 1.206. Such value of St_2 deviates from the dominant $f_1 = 1.25$ by only 4.7%.

Hence, this close agreement implies that the mounting of *EP*3 or *EP*4 panel in the present cavity still allows the original type of Rossiter aeroacoustic coupling [Fig. 10(b)] to happen but within an effective narrower cavity of the same depth even though all the processes involved in the coupling are suppressed as discussed. This clearly shows that the intended actions of respecting the prevalent flow processes by keeping the basic cavity shape intact with strategic modification of aeroacoustic coupling for overall noise suppression, as stated in Sec. IV A, are successfully achieved with *EP*3 and *EP*4 panels.

VI. AEROACOUSTIC–PANEL INTERACTION

It is interesting to see how the acoustically, or aeroacoustically, induced vibration of the elastic panel contributes to the coupling between the developing shear layer and cavity mode in each case. Figure 16 shows the time traces (first column) and the corresponding spectra (second column) pressure fluctuations acting at the mid-points of the panels compared with the pressure fluctuations at the same locations in the *RC* case. The figure shows that the aeroacoustic–structural interaction modifies the coupling to a different extent. When the elastic panel is installed near the cavity leading edge, its aeroacoustically induced vibration is effective in reducing the pressure fluctuation through structural resonance at the designed frequency giving rise to a 20% reduction in magnitude for both *EP*1 and *EP*2 cases. In the *EP*3 case, the acoustically induced vibration of the elastic panel effectively absorbs incident fluctuation energy at the designed panel frequency from shear layer impingement and leaves much less amount of energy than the *RC* case fed back to close the coupling by excitation of shear layer formation. As a result, the reduction of acoustic pressure on the cavity bottom is high as 52%. Similarly, the *EP*4 panel case reduces the acoustic pressure fluctuation due to flow–panel interaction by almost 60%. As such, less energy radiates toward the rigid cavity bottom for the formation of a standing wave, so less acoustic energy is fed back to the cavity leading edge to close the coupling. These observations reveal that effective direct absorption of acoustic pressure at the designed panel resonant frequency would leave nonlinear acoustic–structural interaction essentially at frequencies other than panel resonant one to complete the coupling. This might be the reason why a change of dominant radiation frequency prevails in *EP*3 and *EP*4 cases. In the *EP*5 case, the nonlinear aeroacoustic–panel interaction gives a 30% increase in pressure fluctuation magnitude at the designed panel frequency and sizable contributions at other frequency peaks. They give rise to a strong coupling and a much louder cavity noise as a result. The third column of Fig. 16 depicts the pressure magnitudes along the panels of all cases. The pressure magnitudes in *EP*1 and *EP*2 cases give good support to the delay of shear layer growth due to the modified coupling discussed in Sec. V A. The significant reduction of acoustic pressure from the panels in *EP*3 and *EP*4 cases is noticeable. In the *EP*5 case, the intensification of pressure fluctuation by nonlinear aeroacoustic–panel interaction is fairly uniform along the panel.

Figure 17 shows the temporal displacements of all panels together with their vibratory acceleration spectra obtained from panel mid-points. Evidently, the *EP*1 panel responds to vibrate at the designed resonant frequency. The standing wave pattern in the third fluid-loaded panel resonant mode along the panel persists over time with minor contributions from its two lower-order modes. A similar standing wave pattern prevails in the *EP*2 panel, but it is highly skewed by the emergence of a traveling bending wave bouncing between two ends of the panel at a frequency very close to the first panel resonant mode, which is thus also excited. The *EP*2 panel is entirely embedded in the region for acoustically excited shear layer formation, so it gives a much stronger vibratory response than the *EP*1 panel. These two observations reveal that the panels are able to absorb energy from flow unsteadiness around the cavity leading edge as desired to sustain their resonant vibration. However, the presence of a traveling bending wave in the *EP*2 panel might make its energy absorption by its standing wave counterpart less effective, so the overall modification of the coupling between the shear layer and cavity mode is comparable to the *EP*1 case.

It was illustrated in Sec. V that the panels in *EP*3 and *EP*4 cases act to modify the cavity aeroacoustic coupling in such a way that the cavity Rossiter feedback mechanism operates in an effective narrower cavity of the same depth and results in the flow fluctuations dominant frequency shifted from $f = 0.925$ to $f = 1.25$. Coincidently, the new dominant frequency matches the fourth mode of the resonant panel frequency (Table IV), but the panel responses in *EP*3 and *EP*4 cases are completely different. The entire length of the *EP*3 panel responds to the incident acoustic excitation in a way that its vibratory displacement is coherent along its length (Fig. 17). It vibrates like a rigid body rather than locked into any of its natural panel resonant modes. Nevertheless, a sustained standing wave on the panel is still obvious. Compared to the *EP*1 case, the stronger response of the *EP*3 panel imparts stronger energy absorption for its more effective weakening of feedback processes for closing the coupling and consequently lower overall cavity noise radiation. Its new characteristic frequency of aeroacoustic feedback appears to excite a new cavity mode with a shorter quarter wavelength than in the *EP*1 case (Fig. 15). Similar observations can be made in the *EP*4 case. Owing to highly unsteady flow–panel interaction upon shear layer impingement, the panel responds to lock its vibration into the fourth panel resonant mode with mild contributions from its second and third modes. Although the panel vibratory response of the *EP*4 panel is stronger, its energy absorption is less effective due to the more complex standing wave pattern of shorter wavelengths, so the weakening of feedback processes for aeroacoustic closing the coupling is comparable to the *EP*3 case. The *EP*5 panel is directly exposed to the strong unsteady pressure fluctuations of the flow after shear layer impingement. It gives a sustained standing wave pattern similar to the *EP*1 case but with the strongest vibratory response among all cases.

VII. CONCLUSIONS

This paper reports a unique passive control concept for deep cavity noise suppression using localized surface compliance by invoking the flow-induced structural resonance of an elastic panel embedded in cavity walls. The concept is thoroughly studied with the tonal noise response of a deep cavity of the length-to-depth ratio of 0.4 exposed to a flow of Mach number $M = 0.09$ and Reynolds number $Re = 4 \times 10^4$. The rigid cavity flow characteristics are taken as the basic framework for the elastic panel design. Subsequently, various panel–cavity configurations built on strategically mounted panel locations are attempted to study the effectiveness of the proposed idea for cavity noise suppression.

The spatiotemporal aeroacoustic–structural interaction between the elastic panel and fluid resonant fluctuations of the deep cavity is numerically studied using direct aeroacoustic simulation in two

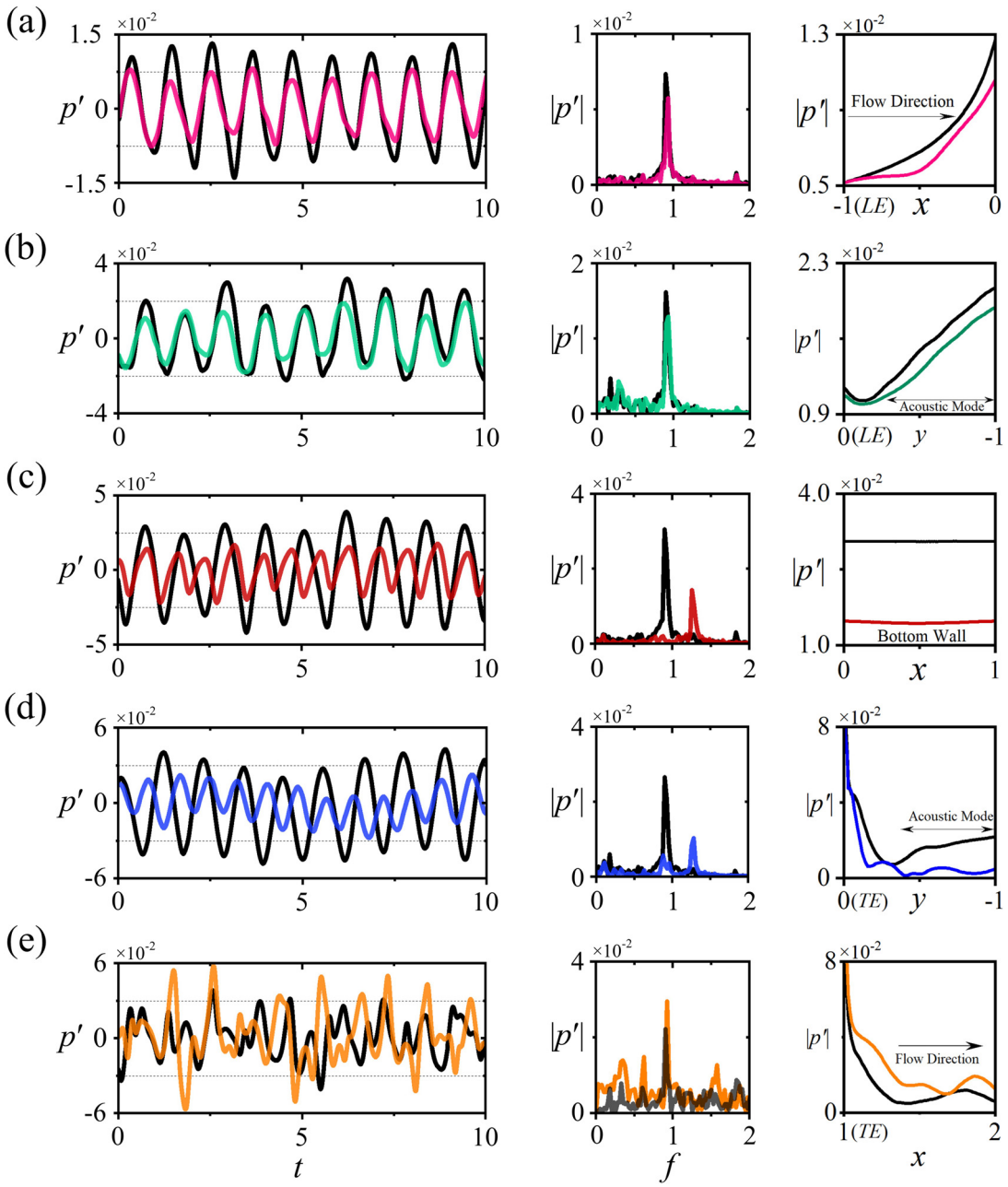

FIG. 16. Temporal (first column) and spectral (second column) distribution of the pressure instabilities at the midpoint of the flow–panel interface and spatial variance of pressure fluctuation (third column) across the panel length and compared with the rigid wall (in black) of (a) *EP*1, (b) *EP*2, (c) *EP*3, (d) *EP*4, and (e) *EP*5.

dimensions. After validation with existing experimental results, the numerical solution of flow past a fully rigid deep cavity is thoroughly studied by means of comprehensive wavenumber–frequency analyses. The same type of interaction between the developing shear layer and cavity acoustic mode and its eventual noise radiation to far-field, as reported in existing numerical and experimental works, is identified from the numerical solution. All the five key flow processes of the cavity aeroacoustic feedback are deciphered, namely, the boundary layer growth upstream of the cavity leading edge, acoustically excited shear layer growth, cavity acoustic standing wave formation, excitation of cavity mode by shear layer impingement at the cavity trailing edge, and the highly unsteady flow subsequent to the shear layer impingement. The elastic panel is assumed to be made of elastomeric material, and its structural properties are designed to ensure that one of its

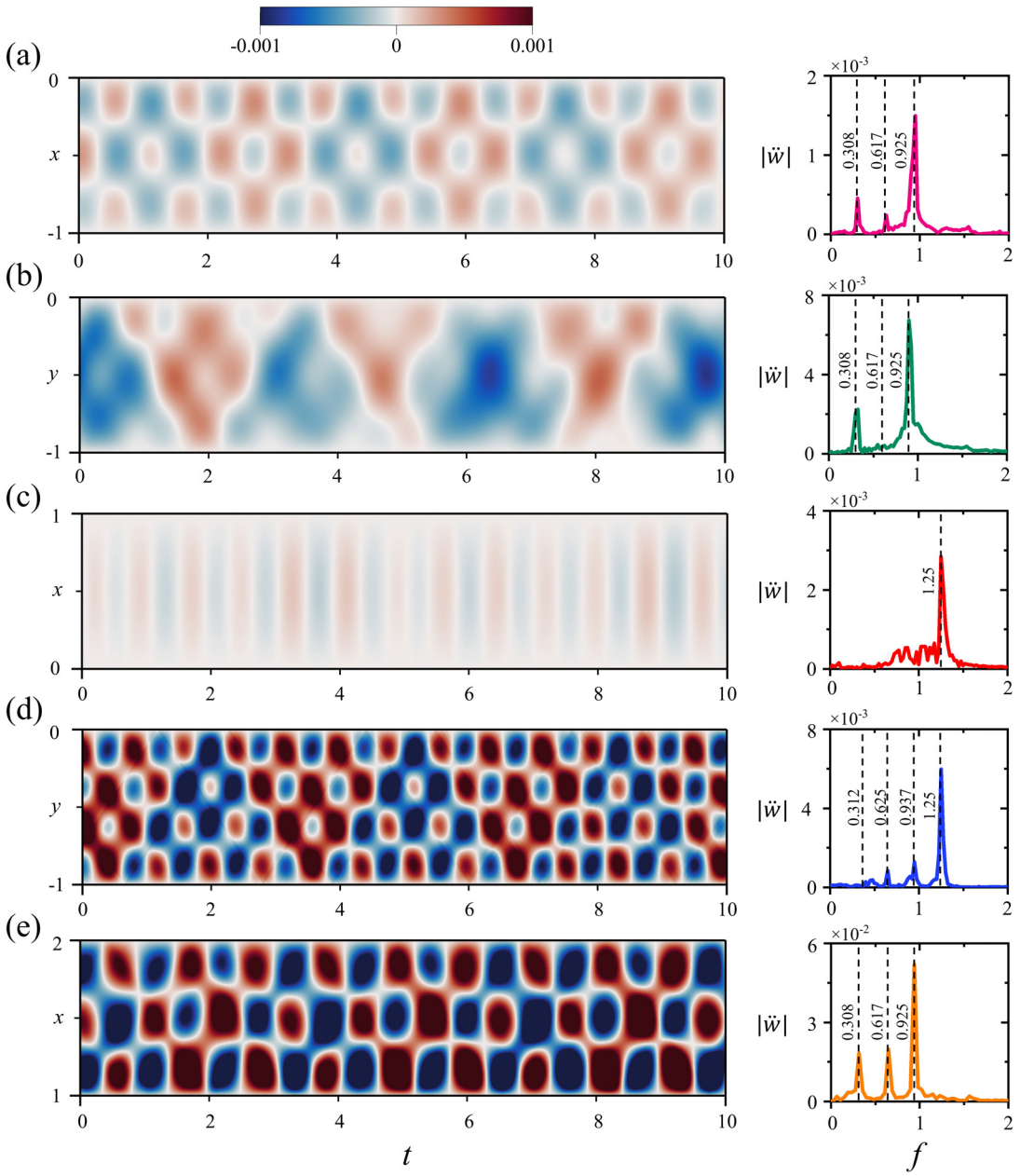

FIG. 17. Panel vibratory responses: (a) *EP*1, (b) *EP*2, (c) *EP*3, (d) *EP*4, and (e) *EP*5. The dashed vertical lines show the first four panel modal frequencies predicted with Eq. (3) with $n = 1, 2, 3$, and 4.

fluid-loaded natural frequencies is equal to the dominant frequency of the resonant flow fluctuation of the rigid cavity. The panel is then strategically set to be exposed to each of the key flow processes identified so as to ascertain its effects on the modification of every process for cavity noise suppression. Panel structural resonance prevails in all cases. The interaction with the first four flow processes for the cavity aeroacoustic feedback gives noise suppression to a different extent, but that with the fifth process gives noise amplification. Significant noise suppression can be obtained with a panel that is allowed to modify the cavity acoustic standing wave formation or excitation of cavity mode by shear layer impingement at the cavity trailing edge. Both are able to give the reduction in cavity noise pressure level and power level up to 3.8 and 4.8 dB, respectively.

An extensive study of the physical mechanism behind the noise suppression cases reveals that the presence of the elastic panel completely alters the aeroacoustic coupling of the key flow processes

responsible for cavity flow resonant fluctuation. The coherency between the shear layer growth and cavity mode acoustics, as observed in the rigid cavity, is grossly weakened due to the imposed surface compliance. That results in a change of the dominant frequency of cavity aeroacoustic feedback to a higher value. The loss in coherency is almost complete in the proximity of the cavity leading edge, so the growth of the shear layer is effectively delayed to further downstream of it. It leads to the occurrence of cavity aeroacoustic feedback in an effective narrower cavity of the same depth. The associated flow processes of the aeroacoustic coupling are weakened by the structurally vibrating resonant panel, so the eventual cavity flow noise is reduced. Further analysis of the aeroacoustic–structural interaction of the panel provides the details of how it responds to absorb the flow and acoustic fluctuation energies. Successful noise suppression comes with an unforeseen advantage. The presence of the panel gives rise to a reduction of overall cavity drag by almost 19% from its rigid cavity counterpart, which may be helpful in reducing the consumption of flow energy required to drive the cavity flow. Therefore, the present paper confirms the feasibility of the proposed use of strategically placed surface compliance that is effective not only in modifying the fundamental deep cavity tonal noise mechanism but also in achieving noise suppression and drag reduction to the cavity yet retaining the basic problem geometry intact. All these features are considered important in many practical applications. Although the present work is carried out at $M = 0.09$ only, it is envisaged that the same approach is applicable to the suppression of deep cavity noise at low to mid Mach numbers for the similarity of their aeroacoustic generation mechanism.

ACKNOWLEDGMENTS

The authors gratefully acknowledge the support from the Research Grants Council of the Government of Hong Kong Special Administrative Region under Grant No. 15208520. The first author is grateful to the stipend support to his study tenable at Department of Mechanical Engineering, The Hong Kong Polytechnic University.

AUTHOR DECLARATIONS

Conflict of Interest

The authors have no conflicts to disclose.

Author Contributions

Muhammad Rehan Naseer: Formal analysis (equal); Investigation (equal); Methodology (equal); Validation (equal); Writing – original draft (lead); Writing – review & editing (equal). **Muhammad Irsalan Arif:** Formal analysis (equal); Investigation (equal); Methodology (equal); Supervision (equal); Writing – review & editing (equal). **Randolph C. K. Leung:** Conceptualization (equal); Funding acquisition (lead); Methodology (equal); Project administration (lead); Resources (equal); Supervision (equal); Writing – review & editing (equal). **Garret C. Y. Lam:** Conceptualization (equal); Methodology (equal); Resources (equal); Software (equal).

DATA AVAILABILITY

The data that support the findings of this study are available from the corresponding author upon reasonable request.

REFERENCES

Abdelmwgoud, M. and Mohany, A., "Control of the self-sustained shear layer oscillations over rectangular cavities using high-frequency vortex generators," Phys. Fluids **33**(4), 045115 (2021).
Arif, I., Lam, G. C. Y., Leung, R. C. K., and Naseer, M. R., "Distributed surface compliance for airfoil tonal noise reduction at various loading conditions," Phys. Fluids **34**(4), 046113 (2022).
Arif, I., Leung, R. C. K., and Naseer, M. R., "A computational study of trailing edge noise suppression with embedded structural compliance," JASA Express Lett. **3**(2), 023602 (2023).
Arif, I., Lam, G. C. Y., Wu, D., and Leung, R. C. K., "Passive airfoil tonal noise reduction by localized flow-induced vibration of an elastic panel," Aerosp. Sci. Technol. **107**, 106319 (2020).
Arya, N. and De, A., "Effect of vortex and entropy sources in sound generation for compressible cavity flow," Phys. Fluids **33**(4), 046107 (2021).
Bies, D. A., Hansen, C. H., and Howard, C. Q., *Engineering Noise Control*, 4th ed. (CRC Press, 2017).
Blevins, R. D., *Formulas for Dynamics, Acoustics and Vibration* (John Wiley and Sons, 2015).
Bruggeman, J. C., Hirschberg, A., van Dongen, M. E. H., Wijnands, A. P. J., and Gorter, J., "Flow induced pulsations in gas transport systems: Analysis of the influence of closed side branches," J. Fluids Eng. **111**(4), 484–491 (1989).
Bruggeman, J. C., Hirschberg, A., van Dongen, M. E. H., Wijnands, A. P. J., and Gorter, J., "Self-sustained aero-acoustic pulsations in gas transport systems: Experimental study of the influence of closed side branches," J. Sound Vib. **150**(3), 371–393 (1991).
Cattafesta, L. N. III, Song, Q., Williams, D. R., Rowley, C. W., and Alvi, F. S., "Active control of flow-induced cavity oscillations," Prog. Aerosp. Sci. **44**(7–8), 479–502 (2008).
Covert, E. E., "An approximate calculation of the onset velocity of cavity oscillations," AIAA J. **8**(12), 2189–2194 (1970).
Dowell, E. H., *Aeroelasticity of Plates and Shells* (Springer Science and Business Media, 1974), Vol. 1.
Dowling, A. P. and Ffowcs Williams, J. E., *Sound and Sources of Sound* (E. Horwood, 1983).
East, L. F., "Aerodynamically induced resonance in rectangular cavities," J. Sound Vib. **3**(3), 277–287 (1966).
El Hassan, M., Keirsbulck, L., and Labraga, L., "Aero-acoustic coupling inside large deep cavities at low-subsonic speeds," J. Fluids Eng. **131**(1), 011204 (2008).
Fan, H. K., Leung, R. C. K., and Lam, G. C. Y., "Numerical analysis of aeroacoustic-structural interaction of a flexible panel in uniform duct flow," J. Acoust. Soc. Am. **137**(6), 3115–3126 (2015).
Fan, H. K., Leung, R. C. K., Lam, G. C. Y., Aurégan, Y., and Dai, X., "Numerical coupling strategy for resolving in-duct elastic panel aeroacoustic/structural interaction," AIAA J. **56**(12), 5033–5040 (2018).
Forestier, N., Jacquin, L., and Geffroy, P., "The mixing layer over a deep cavity at high-subsonic speed," J. Fluid Mech. **475**, 101–145 (2003).
Galbally, D., García, G., Hernando, J., Sánchez, J. de D., and Barral, M., "Analysis of pressure oscillations and safety relief valve vibrations in the main steam system of a boiling water reactor," Nucl. Eng. Des. **293**, 258–271 (2015).
Gharib, M. and Roshko, A., "The effect of flow oscillations on cavity drag," J. Fluid Mech. **177**, 501–530 (1987).
Han, S., Luo, Y., Li, H., Wu, C., Liu, X., and Zhang, S., "Data-driven and physical property-based hydro-acoustic mode decomposition," Phys. Fluids **34**(2), 026102 (2022).
Heller, H. H. and Bliss, D. B., "Aerodynamically induced pressure oscillations in cavities - physical mechanisms and suppression concepts," Technical Report No. AFFDL-TR-74-133 (AF Flight Dynamics Laboratory (FY), Wright-Patterson AFB, OH, 1975).
Ho, Y. W. and Kim, J. W., "A wall-resolved large-eddy simulation of deep cavity flow in acoustic resonance," J. Fluid Mech. **917**, A17 (2021).
Kato, C. and Ikegawa, M., "Large eddy simulation of unsteady turbulent wake of a circular cylinder using the finite element method," in *Advances in Numerical Simulation of Turbulent Flows: Proceedings of the Symposium, ASME and JSME Joint Fluids Engineering Conference* (ASME, 1991), pp. 49–56.

Kook, H., Mongeau, L., Brown, D. V., and Zorea, S. I., "Analysis of the interior pressure oscillations induced by flow over vehicle openings," Noise Control Eng. J. **45**, 223–234 (1997).
Kusano, K., Yamada, K., and Furukawa, M., "Aeroacoustic simulation of broadband sound generated from low-Mach-number flows using a lattice Boltzmann method," J. Sound Vib. **467**, 115044 (2020).
Lam, G. C. Y., Leung, R. C. K., and Tang, S. K., "Aeroacoustics of T-junction merging flow," J. Acoust. Soc. Am. **133**(2), 697–708 (2013).
Lam, G. C. Y., Leung, R. C. K., Seid, K. H., and Tang, S. K., "Validation of CE/SE scheme in low Mach number direct aeroacoustic simulation," Int. J. Nonlinear Sci. Numer. Simul. **15**(2), 157–169 (2014a).
Lam, G. C. Y., Leung, R. C. K., and Tang, S. K., "Aeroacoustics of duct junction flows merging at different angles," J. Sound Vib. **333**(18), 4187–4202 (2014b).
Lam, G. C. Y. and Leung, R. C. K., "Aeroacoustics of NACA 0018 airfoil with a cavity," AIAA J. **56**(12), 4775–4786 (2018).
Larchevêque, L., Sagaut, P., Mary, I., Labbé, O., and Comte, P., "Large-eddy simulation of a compressible flow past a deep cavity," Phys. Fluids **15**(1), 193–210 (2003).
Lee, B. H. K., "Effect of a perturbed shear layer on cavity resonance," J. Aircr. **47**(1), 343–345 (2010).
Leung, R. C. K., So, R. M. C., Wang, M. H., and Li, X. M., "In-duct orifice and its effect on sound absorption," J. Sound Vib. **299**(4–5), 990–1004 (2007).
Li, B., Ye, C.-C., Wan, Z.-H., Liu, N.-S., Sun, D.-J., and Lu, X.-Y., "Noise control of subsonic flow past open cavities based on porous floors," Phys. Fluids **32**(12), 125101 (2020).
Liu, Q. and Gómez, F., "Role of trailing-edge geometry in open cavity flow control," AIAA J. **57**(2), 876–878 (2019).
Liu, Q. and Gaitonde, D., "Acoustic response of turbulent cavity flow using resolvent analysis," Phys. Fluids **33**(5), 056102 (2021).
Mourão Bento, H. F., VanDercreek, C. P., Avallone, F., Ragni, D., and Snellen, M., "Lattice Boltzmann very large eddy simulations of a turbulent flow over covered and uncovered cavities," Phys. Fluids **34**(10), 105120 (2022).
Naseer, M. R., Arif, I., Lam, G. C. Y., and Leung, R. C. K., "Effect of flow-induced surface vibration on deep cavity aeroacoustics," AIAA Paper No. 2022-2958, 2022.
Plentovich, E., Stallings, R., Jr., and Tracy, M., "Experimental cavity pressure measure-ments at subsonic and transonic speeds," NASA Technical Paper No. 3358, 1993.
Rockwell, D. and Naudascher, E., "Review—Self-sustaining oscillations of flow past cavities," J. Fluids Eng. **100**(2), 152–165 (1978).
Rossiter, J. E., "Wind-tunnel experiments on the flow over rectangular cavities at subsonic and transonic speeds," Reports and Memoranda No. 3438 (Aeronautical Research Council, 1964).
Rowley, C. W., Colonius, T., and Basu, A. J., "On self-sustained oscillations in two-dimensional compressible flow over rectangular cavities," J. Fluid Mech. **455**, 315–346 (2002).
Saddington, A. J., Thangamani, V., and Knowles, K., "Comparison of passive flow control methods for a cavity in transonic flow," J. Aircr. **53**(5), 1439–1447 (2016).
Sanmiguel-Rojas, E., Jiménez-González, J. I., Bohorquez, P., Pawlak, G., and Martínez-Bazán, C., "Effect of base cavities on the stability of the wake behind slender blunt-based axisymmetric bodies," Phys. Fluids **23**(11), 114103 (2011).
Sato, M., Asada, K., Nonomura, T., Aono, H., Yakeno, A., and Fujii, K., "Mechanisms for turbulent separation control using plasma actuator at Reynolds number of 1.6×10^6," Phys. Fluids **31**(9), 095107 (2019).
Schumacher, K. L., Doolan, C. J., and Kelso, R. M., "The effect of a cavity on airfoil tones," J. Sound Vib. **333**(7), 1913–1931 (2014).
Sun, Y., Taira, K., Cattafesta, L. N., and Ukeiley, L. S., "Biglobal instabilities of compressible open-cavity flows," J. Fluid Mech. **826**, 270–301 (2017).
Sun, Y., Liu, Q., Cattafesta, L. N. III, Ukeiley, L. S., and Taira, K., "Effects of sidewalls and leading-edge blowing on flows over long rectangular cavities," AIAA J. **57**(1), 106–119 (2019).
Tang, Y.-P. and Rockwell, D., "Instantaneous pressure fields at a corner associated with vortex impingement," J. Fluid Mech. **126**, 187–204 (1983).
Yang, Y., Rockwell, D., Lai-Fook Cody, K., and Pollack, M., "Generation of tones due to flow past a deep cavity: Effect of streamwise length," J. Fluids Struct. **25**(2), 364–388 (2009).
Yokoyama, H., Odawara, H., and Iida, A., "Effects of freestream turbulence on cavity tone and sound source," Int. J. Aerosp. Eng. **2016**, 7347106.
Yokoyama, H., Tanimoto, I., and Iida, A., "Experimental tests and aeroacoustic simulations of the control of cavity tone by plasma actuators," Appl. Sci. **7**(8), 790 (2017).
Yokoyama, H., Otsuka, K., Otake, K., Nishikawara, M., and Yanada, H., "Control of cavity flow with acoustic radiation by an intermittently driven plasma actuator," Phys. Fluids **32**(10), 106104 (2020).
Ziada, S. and Bühlmann, E. T., "Self-excited resonances of two side-branches in close proximity," J. Fluids Struct. **6**(5), 583–601 (1992).
Ziada, S., Oengören, A., and Vogel, A., "Acoustic resonance in the inlet scroll of a turbo-compressor," J. Fluids Struct. **16**(3), 361–373 (2002).
Ziada, S., "Flow-excited acoustic resonance in industry," J. Pressure Vessel Technol. **132**(1), 015001 (2010).